Minimum Norm Least-Squares Wavelet Filtering for Incomplete Geophysical Time Series

Kunpu Ji, Yunzhong Shen, and Fengwei Wang

***Abstract*—Geophysical time series derived from remote sensing and ground-based observations contain rich signals reflecting diverse Earth processes. Wavelet filtering is widely employed to extract these signals from noisy datasets. However, due to many factors, geophysical time series inevitably contain missing data, complicating the direct use of wavelet filtering without prior interpolation. The extended wavelet filtering (EWF) method (Ji et al., 2024) addresses this by linking residuals (signals) to missing data and estimating signals by minimizing the quadratic norm of residuals across both observed epochs and missing epochs. However, EWF is suboptimal for filtering observed data, as residual estimates for missing epochs are less reliable, particularly in time series with consecutive data gaps. This study proposes a new approach, minimum norm least-squares (LS) wavelet filtering (MWF), for processing gappy time series. MWF offers two main advantages over EWF: 1) it filters incomplete time series more effectively through optimal temporal filtering by minimizing the quadratic norm of residuals only for observed epochs. This can avoid disturbances in filtering caused by distorted residuals at missing epochs in EWF. To address the rank deficiency in the parametric model, an additional constraint is applied to minimize the L2-norm of unknown parameters (missing data), ensuring a unique solution and 2) it provides a more concise and effective way to consider prior precision information of the time series by incorporating it into the cost function, without the need for iterative normalization required by the EWF method. We apply the proposed method to extract deformation signals from daily position time series of 27 Global Navigation Satellite System (GNSS) permanent stations in Chinese mainland and compare the results with the EWF method. Results show that MWF outperforms EWF in signal extraction, as indicated by smaller fitting errors and higher signal-to-noise ratios (SNRs). Additional simulations confirm that MWF yields signals closer to the true signals regardless of gap sizes, noise characteristics (pure white or colored noise), and gap distributions (uniform or consecutive).**

***Index Terms*—Geophysical time series, missing data, signal extraction, wavelet filtering.**

I. Introduction

GEOPHYSICAL time series are sequential datasets collected through continuous observation of various physical quantities across different parts of the Earth system. These include measurements such as seismic waves, electromagnetic field variations, geomagnetic changes, and Global Navigation Satellite System (GNSS) displacements [1], [2], [3], [4], [5]. This type of data is valuable for studying the Earth's internal structure and properties, and for understanding natural phenomena like polar glacier melting [6], [7], terrestrial water storage variations [8], [9], [10], [11], snow depth inversion [12], [13], [14], crustal deformation [15], [16], postglacial rebound [17], [18], and sea-level changes [19], [20]. Geophysical time series carry rich signals linked to many geophysical processes. For instance, the horizontal components of GNSS displacements often reveal long-term trends related to tectonic motion [21]. The vertical components typically show seasonal variations caused by environmental loadings [22], [23]. However, these signals are often affected by noise. This includes time-correlated noise at individual stations and spatially correlated noise across multiple stations [24], [25], [26], [27], [28], [29], [30].

Several filtering methods have been developed to extract or remove components within specific frequency bands. Initially, geophysicists employed the Fourier transform (FT) to construct low-, high-, or even-bandpass filtering. However, the FT is only suitable for stationary time series, while most geophysical data exhibit nonstationary behavior [31], [32]. The short-time FT (STFT), introduced by Gabor [33], partially overcomes this limitation by using a sliding window. However, it still struggles to capture signals with multiresolution or rapid variations due to the fixed window size. In the 1980s, researchers developed new mathematical techniques for analyzing time-series data in both the time and frequency domains. Among these, wavelet analysis became a key tool for time–frequency analysis of nonstationary time series, due to its multiscale analysis and computational efficiency. As a result, wavelet analysis gained widespread recognition and use in the scientific community. Although this study focuses on wavelet filtering, we would like to note that there are other analytical methods to model seasonal signals, including fractional Brownian motion (fBm) [34], fractional auto-regressive integrated moving average (FARIMA) model [15], fractional sinusoidal waveform process (fSWp) [35], empirical mode decomposition [26], singular spectrum analysis (SSA) [29], [36], [37], machine learning-based methods [38], Wiener filter [16], Kalman filter [39], weighted nuclear norm minimization (WNNM) [40], truncated nuclear norm regularization (TNNR) [41], and low-rank Hankel completion [42].

Wavelet analysis was originated in geophysics, with Morlet et al. [43], [44] using it for seismic signal analysis. It was later generalized by Grossmann and Morlet [45] and Goupillaud et al. [46], laying the foundation for the continuous wavelet transform (CWT). The discrete wavelet transform (DWT) was then developed and further refined

Received 15 April 2025; revised 6 August 2025 and 11 October 2025; accepted 21 October 2025. Date of publication 27 October 2025; date of current version 17 November 2025. This work was supported in part by the Natural Science Foundation of China under Grant 42274005 and Grant 41974002 and in part by the Program of China Scholarship Council under Grant 202306260236. *(Corresponding author: Yunzhong Shen.)*

The authors are with the College of Surveying and Geo-Informatics, Tongji University, Shanghai 200092, China (e-mail: kunpuji@tongji.edu.cn; yzshen@tongji.edu.cn; wangfw-foster@tongji.edu.cn).

Digital Object Identifier 10.1109/TGRS.2025.3625596

by Daubechies [47], Mallat [48], [49], and Heil and Walnut [50]. Inspired by the pyramid algorithm in image processing, Mallat [48] proposed the multiresolution analysis (MRA). He demonstrated that time series could be decomposed at different scales and accurately reconstructed using a pair of conjugate mirror digital filters. Using MRA, a time series can be decomposed into the time–frequency domain at a given scale, producing several levels of detail coefficients and a level of approximation coefficient via multilevel DWT. The time series can then be filtered by reconstructing it via multilevel inverse DWT (IDWT) using modified coefficients (e.g., setting some coefficients to zero). This method is known as wavelet filtering. Due to its many attractive properties, wavelet analysis has been widely used in various fields, particularly for analyzing geophysical time series like GNSS displacements [1], [51], [52], magnetotelluric data [53], and hyperspectral and multispectral images [54], [55], [56], [57].

However, wavelet analysis requires evenly spaced time series without missing data, which is often not true for geophysical time series due to equipment failure or outlier removal [3], [4]. These gaps pose significant challenges for signal analysis and noise estimation, which are the two main tasks for geophysical time-series analysis [1], [58], [59], [60], [61]. Traditional methods for handling missing data usually involve filling gaps with interpolation, but this approach works only for short gaps and is not appropriate for large, consecutive data gaps. Furthermore, interpolation will introduce marked distortions in the spectral peaks, particularly if the time series is nonstationary [62]. An alternative is to improve existing methods to analyze incomplete time series without interpolation. These methods include improved or modified empirical orthogonal function (EOF)-based techniques with a focus on solving an optimization problem in the frequency domain [37], [58], [59], [63] or spatiotemporal domain [29], [30]. For the wavelet community, various efforts have addressed the challenges of analyzing incomplete time series, including wavelet variance analysis [64], weighted wavelet Z transform (WWZT) [65], and least-squares wavelet analysis (LSWA) [66], [67], [68], [69], [70]. LSWA extends least-squares spectrum analysis (LSSA) from the frequency domain to the time–frequency domain and has demonstrated improved performance over WWZT in detecting time–frequency features in unevenly spaced time series. LSWA achieves excellent performance by applying an appropriate window technique to compute the least-squares wavelet spectrum.

Although LSWA can also estimate signals through windowed least-squares fitting, it differs from conventional wavelet filtering (CWF) based on Mallat's pyramid algorithm, which uses DWT and IDWT. For practical implementation and theoretical background, refer to [1], [71], and [72]. To the best of authors' knowledge, seldom research has been conducted to improve CWF for processing incomplete time series. This study focuses on improving CWF to enable the direct analysis of incomplete data.

Recently, Ji et al. [1] proposed an extended wavelet filtering (EWF) method to directly process time series with missing data based on the LS criterion. The core of the EWF method is to construct a linear equation for the missing data parameters using available observed data and solve it by minimizing the quadratic norm of residuals from both observed and missing epochs. Although the EWF method outperforms traditional wavelet filtering with interpolation, it is suboptimal for filtering observed data, especially for time series with consecutive data gaps, where the residual estimates at missing epochs are less reliable and may even distort the results. Additionally, the method's weighting schemes are not rigorous. The first scheme, which whitens the time series through an iterative process, and the second, which assigns weights to nonexistent observations at missing epochs, both have significant drawbacks.

To address these limitations, we propose a novel approach called minimum norm LS wavelet filtering (MWF), which directly filters gappy time series by minimizing the quadratic norm of residuals only at observed epochs. While the parametric model constructed by this modified criterion is rank deficient, MWF introduces an additional minimum norm constraint to unknown parameters to ensure a unique solution. Unlike EWF, which includes residual constraints for missing epochs, our MWF method allows more effective filtering of observed data without being disturbed by the unstable residuals at missing epochs. Additionally, since the cost function in the MWF method only minimizes residuals for observed epochs, the prior covariance matrix of the time series can be naturally incorporated without the need for iterative normalization as in the EWF method. The rest of this article is organized as follows. Section II describes the proposed methodology, Sections III and IV evaluate the proposed method by comparing it with the EWF and other methods using real GNSS position time series and synthetic data, and Section V presents the conclusions.

II. Methodology

A. Mapping From Time Series to Signals

Let $\boldsymbol{x} = (x_1, x_2, \ldots, x_N)^{\mathrm{T}}$ represent a noisy time series of length N. Using MRA, the original time series $\boldsymbol{x}$ can be decomposed into several detail components $\boldsymbol{d}_i (1 \le i \le J)$ at different scales and the approximation component $\boldsymbol{a}_J$

$$\boldsymbol{x} = \sum_{i=1}^{J} \boldsymbol{d}_i + \boldsymbol{a}_J \tag{1}$$

where $J < [\log_2 N]$ is the decomposition level, with $[\cdot]$ denoting the floor function (rounding down to the nearest integer). According to [48] and [73], $\boldsymbol{d}_i$ represents the detailed component of $\boldsymbol{x}$ within the frequency band $[1/(2^{i+1}\Delta t), 1/(2^i \Delta t)]$, and $\boldsymbol{a}_J$ represents the approximation of $\boldsymbol{x}$ within the frequency band $[0, 1/(2^{J+1}\Delta t)]$, where Δt is the sampling interval. The components $\boldsymbol{d}_i$ and $\boldsymbol{a}_J$ can be obtained using Mallat's pyramid algorithm by applying the multilevel DWT and IDWT. The flowchart of the DWT and IDWT is shown in Appendix A. For further details, refer to [1] and [71].

Previous studies have shown that $\boldsymbol{d}_i$ and $\boldsymbol{a}_J$ are essentially the linear transformation of $\boldsymbol{x}$ [1]. Given that most of the signals are contained in the first few components, we can reconstruct $\boldsymbol{x}$ using

$$\boldsymbol{s} = \sum_{i=r+1}^{J} \boldsymbol{d}_i + \boldsymbol{a}_J = \boldsymbol{A}\boldsymbol{x} \tag{2}$$

where r is the reconstruction level and $\boldsymbol{A}$ is the projection matrix with the elements solely depend on the low (high)-pass filters associated with a chosen mother wavelet. The projection matrix $\boldsymbol{A}$ can be constructed directly by dissecting the multilevel DWT and IDWT procedures. However, this approach has high time and space complexity [1]. Based on the linear projection from $\boldsymbol{x}$ to $\boldsymbol{s}$, we can construct $\boldsymbol{A}$ efficiently in an indirect way

$$\boldsymbol{A} = \boldsymbol{A}\boldsymbol{I}_N = \left(T(\boldsymbol{i}_1) \quad T(\boldsymbol{i}_2) \quad \cdots \quad T(\boldsymbol{i}_N)\right) \tag{3}$$

where $\boldsymbol{i}_k$ is the kth column vector of the $N \times N$ identity matrix $\boldsymbol{I}_N$, and $T(\cdot)$ is the operator for filtering a time series with the specified r using the Mallat pyramid algorithm based on multilevel DWT and IDWT. The flowchart of obtaining matrix $\boldsymbol{A}$ is shown in Appendix B.

There is no rigorous criterion for selecting the reconstruction level r that is suitable for all cases. For daily GNSS position time series, the sampling period $\Delta t = 1$ day $= 1/365.25$ year ≈ 0.0027 year year since $1/365 \in (1/2^9, 1/2^8)$ and $1/182 \in (1/2^8, 1/2^7)$; annual and semiannual oscillations are included in $\boldsymbol{d}_8$ and $\boldsymbol{d}_7$, respectively. These annual and semiannual oscillations dominate the seasonal variation in GNSS position time series [72], [74], so we reconstruct $\boldsymbol{x}$ by summarizing $\boldsymbol{a}_8 + \boldsymbol{d}_8 + \boldsymbol{d}_7$, with r set to 6. In this case, the signals have a frequency band $[0, 1/(2^7\Delta t)]\text{year}^{-1}$. It should be noted that the extracted signals $\boldsymbol{a}_8 + \boldsymbol{d}_8 + \boldsymbol{d}_7$ may not fully reflect all periodic signals in GNSS position time series, as there may exist other smaller periodic oscillations [75]. However, identifying all potential periodic signals is beyond the scope of this study. This study focuses on developing the MWF method and comparing it with the EWF method, using the same reconstruction level.

B. Filtering Time Series With Missing Data

By subtracting $\boldsymbol{s}$ from $\boldsymbol{x}$, we obtain the residuals

$$\boldsymbol{e} = \boldsymbol{x} - \boldsymbol{s} = (\boldsymbol{I}_N - \boldsymbol{A})\,\boldsymbol{x} = \boldsymbol{B}\boldsymbol{x} \tag{4}$$

with $\boldsymbol{B} = \boldsymbol{I}_N - \boldsymbol{A}$. Let S and $\overline{S}$ represent the index sets of observed and missing data in $\boldsymbol{x}$, respectively. The observed and missing data in $\boldsymbol{x}$ are then denoted as $\boldsymbol{x}_1 = \{x_i \mid i \in S\}$ and $\boldsymbol{x}_2 = \{x_i \mid i \in \overline{S}\}$, respectively.

Focusing on the observed parts of $\boldsymbol{s}$ in (2) and $\boldsymbol{e}$ in (4), we obtain

$$\boldsymbol{s}_1 = \boldsymbol{A}_1\boldsymbol{x}_1 + \boldsymbol{A}_2\boldsymbol{x}_2 \tag{5}$$

$$\boldsymbol{e}_1 = \boldsymbol{B}_1\boldsymbol{x}_1 + \boldsymbol{B}_2\boldsymbol{x}_2 \tag{6}$$

where $\boldsymbol{s}_1 = \{s_i \mid i \in S\}$ and $\boldsymbol{e}_1 = \{e_i \mid i \in S\}$. The matrices $\boldsymbol{A}_1 = \{a_{ij} \mid i, j \in S\}$ and $\boldsymbol{A}_2 = \{a_{ij} \mid i \in S, j \in \overline{S}\}$ are the submatrices of $\boldsymbol{A}$, with a_{ij} is the element in the ith row and jth column of $\boldsymbol{A}$. Similarly, $\boldsymbol{B}_1 = \{b_{ij} \mid i, j \in S\}$ and $\boldsymbol{B}_2 = \{b_{ij} \mid i \in S, j \in \overline{S}\}$ are the submatrices of $\boldsymbol{B}$, with b_{ij} being the element in the ith row and jth column of $\boldsymbol{B}$. The sizes of $\boldsymbol{A}_1$ and $\boldsymbol{B}_1$ are $N_S \times N_S$, and the sizes of $\boldsymbol{A}_2$ and $\boldsymbol{B}_2$ are $N_S \times N_{\overline{S}}$, respectively, with N_S and $N_{\overline{S}}$ representing the lengths of S and $\overline{S}$.

To guarantee optimal filtering of observed data, the missing data $\boldsymbol{x}_2$ in (6) can be estimated with the LS criterion

$$\hat{x}_2 = \underset{\boldsymbol{x}_2}{\operatorname{argmin}}\ \|\boldsymbol{e}_1\|^2_{\boldsymbol{I}_{N_S}} = \underset{\boldsymbol{x}_2}{\operatorname{argmin}}\ \boldsymbol{e}_1^{\mathrm{T}}\boldsymbol{e}_1 \tag{7}$$

where $\|\cdot\|^2_{\boldsymbol{Q}} = (\cdot)^{\mathrm{T}}\boldsymbol{Q}(\cdot)$ means the L2-norm operator. Based on the criterion (7), the following normal equation is obtained:

$$-\left(\boldsymbol{B}_2^{\mathrm{T}}\boldsymbol{B}_2\right)\boldsymbol{x}_2 = \boldsymbol{B}_2^{\mathrm{T}}\boldsymbol{y}_1. \tag{8}$$

Here, $\boldsymbol{y}_1 = \boldsymbol{B}_1\boldsymbol{x}_1$. However, the rank of the coefficient matrix $\boldsymbol{B}_2$ is no greater than $N_{\overline{S}}$, i.e., $\text{Rank}(\boldsymbol{B}_2) \le N_{\overline{S}}$, where $\text{Rank}(\cdot)$ is the operator to compute the rank of a matrix. In most cases, $\boldsymbol{B}_2$ is rank-deficient; specifically, as mathematically proven in Appendix C, when the percentage of missing data exceeds 50%, $\boldsymbol{B}_2$ becomes rank-deficient. For cases where the percentage of missing data is below 50%, while a mathematical proof of whether $\boldsymbol{B}_2$ is rank-deficient or full column rank is unavailable, extensive numerical experiments (also detailed in Appendix C) have shown that $\boldsymbol{B}_2$ achieves full column rank only when the missing rate is extremely low, such as 1%. In most other scenarios, $\boldsymbol{B}_2$ remains rank-deficient, with the degree of rank deficiency increasing as the missing rate rises. Therefore, there is no guarantee that (8) has a unique solution.

To ensure a unique solution, we introduce an additional constraint

$$\min: \|\boldsymbol{x}_2\|^2_{\boldsymbol{I}_{N_{\overline{S}}}} = \min: \boldsymbol{x}_2^{\mathrm{T}}\boldsymbol{x}_2. \tag{9}$$

To solve the optimization problem in (9), we construct the following target function:

$$\Phi(\boldsymbol{x}_2, \boldsymbol{\lambda}) = \boldsymbol{x}_2^{\mathrm{T}}\boldsymbol{x}_2 + 2\boldsymbol{\lambda}^{\mathrm{T}}\left(\boldsymbol{B}_2^{\mathrm{T}}\boldsymbol{y}_1 + \boldsymbol{B}_2^{\mathrm{T}}\boldsymbol{B}_2\boldsymbol{x}_2\right) \tag{10}$$

where $\boldsymbol{\lambda}$ is an $N_{\overline{S}} \times 1$ vector of Lagrange multipliers. Using the Euler–Lagrange theorem, we have

$$\frac{1}{2}\frac{\partial\Phi}{\partial\boldsymbol{x}_2} = \boldsymbol{x}_2 + \boldsymbol{B}_2^{\mathrm{T}}\boldsymbol{B}_2\boldsymbol{\lambda} = \boldsymbol{0} \tag{11}$$

$$\frac{1}{2}\frac{\partial\Phi}{\partial\boldsymbol{\lambda}} = \boldsymbol{B}_2^{\mathrm{T}}\boldsymbol{y}_1 + \boldsymbol{B}_2^{\mathrm{T}}\boldsymbol{B}_2\boldsymbol{x}_2 = \boldsymbol{0}. \tag{12}$$

From (11), we find

$$\boldsymbol{x}_2 = -\boldsymbol{B}_2^{\mathrm{T}}\boldsymbol{B}_2\boldsymbol{\lambda}. \tag{13}$$

Substituting (13) into (12), we obtain

$$\boldsymbol{B}_2^{\mathrm{T}}\boldsymbol{y}_1 - \boldsymbol{B}_2^{\mathrm{T}}\boldsymbol{B}_2\boldsymbol{B}_2^{\mathrm{T}}\boldsymbol{B}_2\boldsymbol{\lambda} = 0. \tag{14}$$

Since $\text{Rank}(\boldsymbol{B}_2^{\mathrm{T}}\boldsymbol{B}_2\boldsymbol{B}_2^{\mathrm{T}}\boldsymbol{B}_2) = \text{Rank}(\boldsymbol{B}_2)$, the matrix $\boldsymbol{B}_2^{\mathrm{T}}\boldsymbol{B}_2\boldsymbol{B}_2^{\mathrm{T}}\boldsymbol{B}_2$ is rank-deficient. Thus, we can acquire

$$\boldsymbol{\lambda} = \left(\boldsymbol{B}_2^{\mathrm{T}}\boldsymbol{B}_2\boldsymbol{B}_2^{\mathrm{T}}\boldsymbol{B}_2\right)^{+}\boldsymbol{B}_2^{\mathrm{T}}\boldsymbol{y}_1 \tag{15}$$

where "+" represents the Moore–Penrose inverse. Substituting (15) into (13) and considering the basic property of the Moore–Penrose inverse, we obtain

$$\begin{aligned}\boldsymbol{x}_2 &= -\boldsymbol{B}_2^{\mathrm{T}}\boldsymbol{B}_2\left(\boldsymbol{B}_2^{\mathrm{T}}\boldsymbol{B}_2\boldsymbol{B}_2^{\mathrm{T}}\boldsymbol{B}_2\right)^{+}\boldsymbol{B}_2^{\mathrm{T}}\boldsymbol{y}_1 \\ &= -\left(\boldsymbol{B}_2^{\mathrm{T}}\boldsymbol{B}_2\right)^{+}\boldsymbol{B}_2^{\mathrm{T}}\boldsymbol{y}_1 \\ &= -\boldsymbol{B}_2^{+}\boldsymbol{y}_1.\end{aligned} \tag{16}$$

When $\boldsymbol{B}_2$ is full column rank, (16) degenerates into the LS solution $\boldsymbol{x}_2 = -(\boldsymbol{B}_2^{\mathrm{T}}\boldsymbol{B}_2)^{-1}\boldsymbol{B}_2^{\mathrm{T}}\boldsymbol{y}_1$. This shows that the LS solution also satisfies the minimum norm property. Therefore, the minimum norm constraint (9) we added is general and applicable to all cases of $\text{Rank}(\boldsymbol{B}_2)$. Finally, by substituting (16) into (5), we obtain

$$\boldsymbol{s}_1 = \left(\boldsymbol{A}_1 - \boldsymbol{A}_2\boldsymbol{B}_2^{+}\boldsymbol{B}_1\right)\boldsymbol{x}_1. \tag{17}$$

If the prior precision for the time series is available, it should be incorporated to improve filtering performance. Let $\boldsymbol{\Sigma}$ represent the variance–covariance matrix of $\boldsymbol{x}_1$. We start with decomposing $\boldsymbol{\Sigma}$ as $\boldsymbol{\Sigma} = \boldsymbol{L}\boldsymbol{L}^{\mathrm{T}}$, where $\boldsymbol{L}$ is a lower triangular matrix. In this case, (6) can be rewritten as

$$\overline{\boldsymbol{e}}_1 = \overline{\boldsymbol{y}}_1 + \overline{\boldsymbol{B}}_2\boldsymbol{x}_2 \tag{18}$$

where $\overline{\boldsymbol{e}}_1 = \boldsymbol{L}^{-1}\boldsymbol{e}_1, \overline{\boldsymbol{y}}_1 = \boldsymbol{L}^{-1}\boldsymbol{y}_1$, and $\overline{\boldsymbol{B}}_2 = \boldsymbol{L}^{-1}\boldsymbol{B}_2$. It is easy to prove that $\overline{\boldsymbol{e}}_1$ is homogeneous, meaning that $D(\overline{\boldsymbol{e}}_1) = \boldsymbol{I}_{N_S}$, where $D(\cdot)$ denotes the dispersion operator. Similarly, using the weighted LS criterion in the following equation:

$$\text{min: } \|\overline{\boldsymbol{e}}_1\|^2_{\boldsymbol{I}_{N_S}} = \text{min: } \|\boldsymbol{e}_1\|^2_{\boldsymbol{\Sigma}^{-1}} = \text{min: } \boldsymbol{e}_1^{\mathrm{T}}\boldsymbol{\Sigma}^{-1}\boldsymbol{e}_1 \tag{19}$$

we can derive the normal equation

$$-\left(\overline{\boldsymbol{B}}_2^{\mathrm{T}}\overline{\boldsymbol{B}}_2\right)\boldsymbol{x}_2 = \overline{\boldsymbol{B}}_2^{\mathrm{T}}\overline{\boldsymbol{y}}_1. \tag{20}$$

With the minimum norm constraint from (9), we have

$$\hat{\boldsymbol{x}}_2 = -\overline{\boldsymbol{B}}_2^{+}\overline{\boldsymbol{y}}_1 \tag{21}$$

$$\boldsymbol{s}_1 = \left(\boldsymbol{A}_1 - \boldsymbol{A}_2\overline{\boldsymbol{B}}_2^{+}\overline{\boldsymbol{B}}_1\right)\boldsymbol{x}_1 \tag{22}$$

where $\overline{\boldsymbol{B}}_1 = \boldsymbol{L}^{-1}\boldsymbol{B}_1$.

Specifically, for GNSS position time series, only the square roots of the diagonal elements of $\boldsymbol{\Sigma}$, known as the formal errors σ_i, are available. In this case, $\boldsymbol{L}$ is a diagonal matrix with the formal errors as its diagonal elements.

The Moore–Penrose inverse of $\boldsymbol{B}_2$ is computed using the singular value decomposition (SVD) (assuming $N_S \geq N_{\overline{S}}$)

$$\boldsymbol{B}_2 = \boldsymbol{U}\boldsymbol{\Lambda}\boldsymbol{V}^{\mathrm{T}} = \sum_{i=1}^{N_{\overline{S}}}\lambda_i\boldsymbol{u}_i\boldsymbol{v}_i^{\mathrm{T}} \tag{23}$$

where $\boldsymbol{U}$ is an $N_S \times N_{\overline{S}}$ matrix with $\boldsymbol{U}^{\mathrm{T}}\boldsymbol{U} = \boldsymbol{I}_{N_{\overline{S}}}$ and $\boldsymbol{u}_i$ is its ith column vector; $\boldsymbol{\Lambda}$ is an $N_{\overline{S}} \times N_{\overline{S}}$ diagonal matrix with singular values λ_i, sorted in descending order; and $\boldsymbol{V}$ is an $N_{\overline{S}} \times N_{\overline{S}}$ orthogonal matrix, satisfying $\boldsymbol{V}\boldsymbol{V}^{\mathrm{T}} = \boldsymbol{V}^{\mathrm{T}}\boldsymbol{V} = \boldsymbol{I}_{N_{\overline{S}}}$. When $\boldsymbol{B}_2$ is rank-deficient, the number of rank deficiencies is $N_r = N_{\overline{S}} - \mathrm{Rank}(\boldsymbol{B}_2)$. This means the last N_r singular values are zero. The Moore–Penrose inverse of $\boldsymbol{B}_2$ is then expressed as

$$\boldsymbol{B}_2^{+} = \boldsymbol{V}\boldsymbol{\Lambda}^{+}\boldsymbol{U}^{\mathrm{T}} = \sum_{i=1}^{\mathrm{Rank}(\boldsymbol{B}_2)}\frac{1}{\lambda_i}\boldsymbol{v}_i\boldsymbol{u}_i^{\mathrm{T}}. \tag{24}$$

However, determining $\mathrm{Rank}(\boldsymbol{B}_2)$ is theoretically nearly impossible. Moreover, due to numerical errors, the smaller singular values approach zero but are rarely exactly zero. To address this, a common method is to use a tolerance (tor) to distinguish between nonzero and zero singular values. Singular values smaller than tor are treated as zero. This study adopts MATLAB's built-in default tor, employed in its "rank" and "pinv" functions for computing the rank and Moore–Penrose inverse of a matrix

$$\mathrm{tor} = \max\left(N_S, N_{\overline{S}}\right) \times 2^{\lceil\log_2(\lambda_1)\rceil - 52} \tag{25}$$

where $\max(a, b)$ returns the larger of a and b. Based on this criterion, $\mathrm{Rank}(\boldsymbol{B}_2) = \max(\{i \mid \lambda_i > \mathrm{tor}\})$. For the case of $N_S < N_{\overline{S}}$, we first compute $(\boldsymbol{B}_2^{\mathrm{T}})^{+}$ using (23)–(25) and then compute its transpose. A detailed flowchart of the proposed MWF method is presented in Appendix D.

C. Merits of the MWF Method Relative to the EWF Method

Focusing on the components at the missing epochs in (2)–(4), we have

$$\boldsymbol{s}_2 = \boldsymbol{A}_3\boldsymbol{x}_1 + \boldsymbol{A}_4\boldsymbol{x}_2 \tag{26}$$

$$\boldsymbol{e}_2 = \boldsymbol{B}_3\boldsymbol{x}_1 + \boldsymbol{B}_4\boldsymbol{x}_2. \tag{27}$$

Here, $\boldsymbol{A}_3 = \{a_{ij} \mid i \in \overline{S}, j \in S\}$ and $\boldsymbol{A}_4 = \{a_{ij} \mid i \in \overline{S}, j \in \overline{S}\}$ are the submatrices of $\boldsymbol{A}$, with sizes $N_{\overline{S}} \times N_S$ and $N_{\overline{S}} \times N_{\overline{S}}$, respectively. Similarly, $\boldsymbol{B}_3 = \{b_{ij} \mid i \in \overline{S}, j \in S\}$ and $\boldsymbol{B}_4 = \{b_{ij} \mid i \in \overline{S}, j \in S\}$ are the submatrices of $\boldsymbol{B}$ with the same sizes.

In the EWF method [1], the missing data $\boldsymbol{x}_2$ are estimated as

$$\hat{\boldsymbol{x}}_2 = \underset{\boldsymbol{x}_2}{\operatorname{argmin}}\, \boldsymbol{e}_1^{\mathrm{T}}\boldsymbol{e}_1 + \boldsymbol{e}_2^{\mathrm{T}}\boldsymbol{e}_2 = -\left(\boldsymbol{C}_2^{\mathrm{T}}\boldsymbol{C}_2\right)^{-1}\left(\boldsymbol{C}_2^{\mathrm{T}}\boldsymbol{C}_1\boldsymbol{x}_1\right). \tag{28}$$

The corresponding filtered signals of the observed data $\boldsymbol{x}_1$ are

$$\boldsymbol{s}_1 = \left(\boldsymbol{A}_1 - \boldsymbol{A}_2\left(\boldsymbol{C}_2^{\mathrm{T}}\boldsymbol{C}_2\right)^{-1}\boldsymbol{C}_2^{\mathrm{T}}\boldsymbol{C}_1\right)\boldsymbol{x}_1. \tag{29}$$

Here, $\boldsymbol{C}_1 = \{b_{ij} \mid 1 \leq i \leq N, j \in S\}$ and $\boldsymbol{C}_2 = \{b_{ij} \mid 1 \leq i \leq N, j \in \overline{S}\}$ are the submatrices of $\boldsymbol{B}$ with sizes $N \times N_S$ and $N \times N_{\overline{S}}$, respectively. Actually, $\boldsymbol{C}_1$ consists of $\boldsymbol{B}_1$ and $\boldsymbol{B}_3$, while $\boldsymbol{C}_2$ consists of $\boldsymbol{B}_2$ and $\boldsymbol{B}_4$.

From (28), it is evident that the EWF method minimizes residuals at both observed and missing epochs. This additional constraint addresses the rank-deficiency issue of minimizing $\boldsymbol{e}_1^{\mathrm{T}}\boldsymbol{e}_1$. However, the residual $\boldsymbol{e}_2$ does not correspond to actual observations, as no data is observed at the missing epochs. Additionally, as shown in Section III, the filtered signals for missing epochs ($\boldsymbol{s}_2$) are less reliable than those for observed epochs ($\boldsymbol{s}_1$), particularly for time series with consecutive missing data. As a result, the term $\boldsymbol{e}_2^{\mathrm{T}}\boldsymbol{e}_2$ in (28) is not only unnecessary for filtering the observed data $\boldsymbol{x}_1$, but may also degrade the results. In contrast, the proposed MWF method focuses solely on filtering observed data [see (7) or (9) and (19)], avoiding interference from unstable residuals at missing epochs.

Additionally, the MWF method offers a simpler and more effective way to incorporate prior precision of the time series compared to the EWF method. Ji et al. [1] propose two weighting schemes [considering only the formal errors $\sigma_i^2 (i \in S)$].

1) Iteratively homogenizing the time series: $\boldsymbol{x}_1' = \boldsymbol{s}_1 + \boldsymbol{P}_1\boldsymbol{e}_1$, where $\boldsymbol{P}_1$ is a diagonal matrix with elements $\sigma_0/\sigma_i^2 (i \in S)$ and $\sigma_0 = \left(N_S / \sum_{i \in S} 1/\sigma_i^2\right)^{1/2}$. While effective for processing heterogeneous data, this scheme is not a direct solution and may change the reconstruction level during iteration. It is also time-consuming.
2) Directly assigning weights to both observed and missing epochs in the cost function: min: $\boldsymbol{e}_1^{\mathrm{T}}\boldsymbol{P}_1\boldsymbol{e}_1 + \boldsymbol{e}_2^{\mathrm{T}}\boldsymbol{e}_2$. However, this approach raises concerns about assigning weights to nonexistent observations.

The MWF method naturally incorporates the prior covariance matrix into the cost function [see (19)]. Its weighting scheme surpasses that of the EWF method, as it avoids iterative homogenization and the need to assign weights to missing epochs. A detailed comparison between the weighted MWF and weighted EWF methods is presented in Section III.

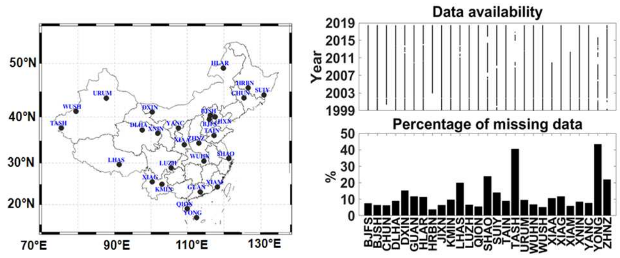

Fig. 1. (Left) Geographic locations of 27 stations and (right) data availability and percentage of missing data.

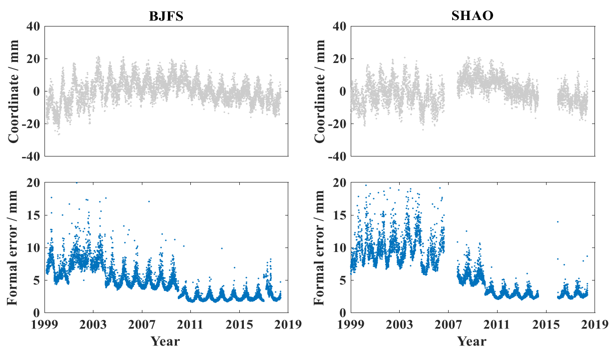

Fig. 2. (Top) Vertical position time series and (bottom) associated formal errors of BJFS and SHAO stations.

III. Experimental Analysis

A. Data Description

To assess the performance of the proposed method, we select the vertical position time series of 27 stations from 1999 to 2019 located in mainland China. Fig. 1 presents the time series and data availability as well as the percentage of missing data. Outliers within the time series are identified using the three times interquartile range (IQR) criterion and subsequently eliminated. In addition, time series with formal errors greater than 20 mm are regarded as outliers. Offsets in time series are detected and repaired using the sigseg tool and manual visual inspection [76].

B. Real Time-Series Analysis

We follow previous studies [1], [51], [77] by employing the Coiflet wavelet with five vanishing moments (Coiflet-5) as the mother wavelet, due to its superior properties including near symmetric and excellent sampling approximation of smooth functions. We first take BJFS and SHAO stations' position time series as examples for illustration. Fig. 2 presents the vertical position time series of the two stations (top row) and the associated formal errors (bottom row). To visualize the time series at different scales, we first fill the data gaps with zeros, and then decompose the time series with $J = 8$. Fig. 3 presents the reconstructed components and the corresponding power spectra for BJFS and SHAO examples. It is clear that $\boldsymbol{a}_8$ represent the nonlinear trend, and $\boldsymbol{d}_8$ and $\boldsymbol{d}_7$ represent the annual and semiannual signals, respectively, which is consistent with the theoretical analysis.

Fig. 4(a) and (b) displays the singular values of the coefficient matrix $\boldsymbol{B}_2$ and the tor computed using (25) for the BJFS and SHAO examples. It is clear that $\text{Rank}(\boldsymbol{B}_2) = 119 < N_{\overline{S}} = 454$ for BJFS and $\text{Rank}(\boldsymbol{B}_2) = 124 < N_{\overline{S}} = 1560$, indicating rank deficiency. The degree of rank deficiency, calculated as $(N_S - \text{Rank}(\boldsymbol{B}_2))/N_S \times 100\%$ is 73.8% for BJFS and 92.1% for SHAO. Fig. 4(c) and (d) displays the singular values of $\boldsymbol{C}_2$ and the tor, showing that $\boldsymbol{C}_2$ is full column rank. This indicates that the additional constraint $\boldsymbol{e}_2^{\mathrm{T}}\boldsymbol{e}_2$ introduced by the EWF method can address the rank deficiency of minimizing only $\boldsymbol{e}_1^{\mathrm{T}}\boldsymbol{e}_1$ although it is not theoretically optimal. Fig. 5(a) and (b) shows the signals extracted by the EWF and MWF methods, and their differences are shown in Fig. 5(c) and (d). The results

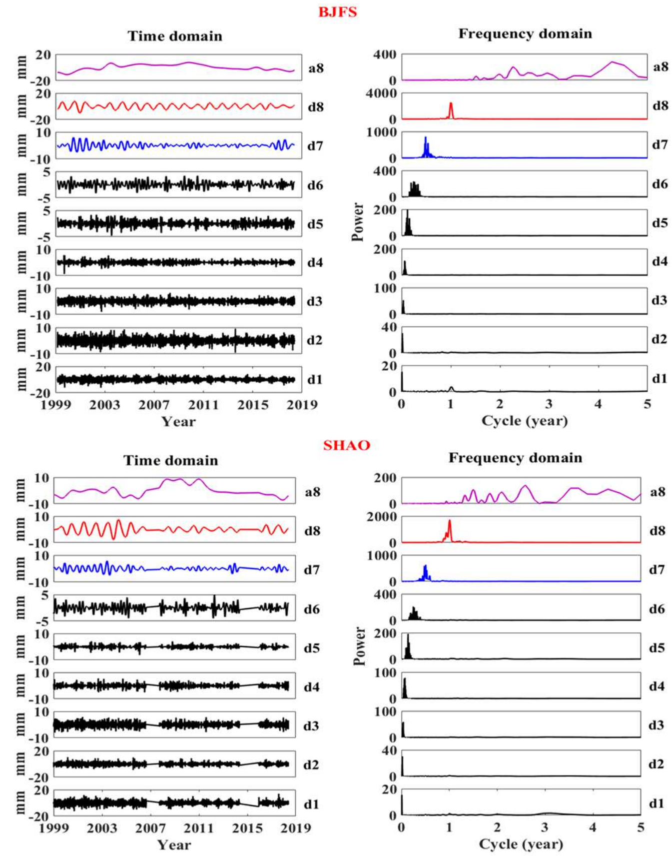

Fig. 3. (Left) Reconstructed components and (right) their power spectral for the BJFS and SHAO examples.

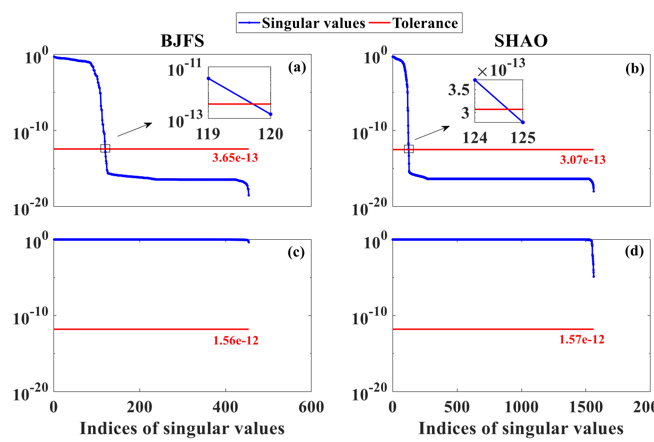

Fig. 4. Singular values of $\boldsymbol{B}_2$ and $\boldsymbol{C}_2$ and the tor. (a) and (b) $\boldsymbol{B}_2$. (c) and (d) $\boldsymbol{C}_2$.

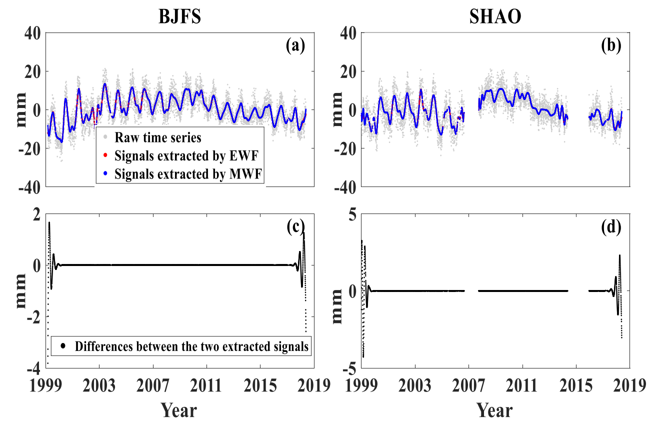

Fig. 5. Signals extracted by EWF and MWF and their differences. (a) and (b) Extracted signals. (c) and (d) Differences.

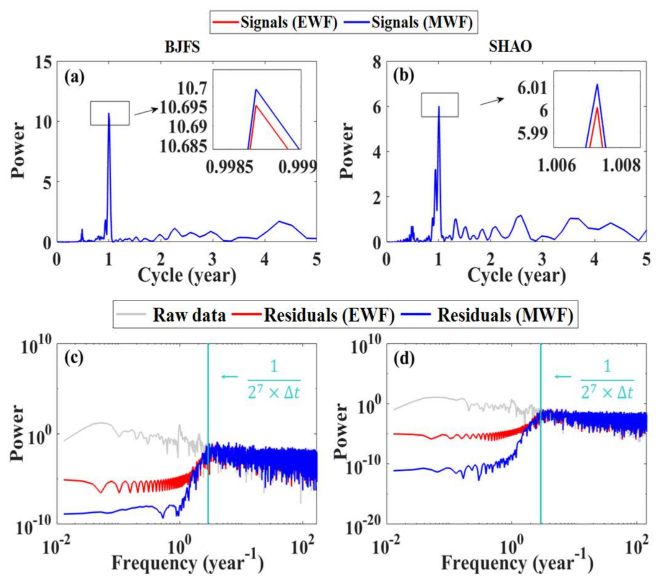

Fig. 6. Power spectra of the extracted signals and the residuals. (a) and (b) Extracted signals. (c) and (d) Raw data and the residuals after subtracting signals.

demonstrate that both methods effectively capture the seasonal variations in the time series, with minimal differences between the two signals except at the endpoints.

Since the two signals are hard to distinguish in the time domain, we calculate the power spectra of the extracted signals using the Lomb–Scargle algorithm [78], [79], as shown in Fig. 6(a) and (b). The results indicate that the power of the signals extracted by the MWF method is higher than that of the EWF method, especially for annual oscillations. We also calculate the power spectra of the raw time series and the residuals after subtracting the extracted signals, as shown in Fig. 6(c) and (d). The results reveal a significant reduction in the power of low-frequency components within the frequency band $[0, 1/(2^7 \times \Delta t)]$ year^{-1}, indicating effective filtering. Moreover, the residual power for the MWF method is much lower than that for the EWF method, showing that the MWF method extracts more signals.

We process the remaining 26 stations using both the MWF and EWF methods. Fig. 7(a) shows the rank of $\boldsymbol{B}_2$ and the number of unknowns (also the column number of $\boldsymbol{B}_2$), and Fig. 7(b) shows the degree of rank deficiency and percentage of missing data. For most stations, the degree of rank deficiency exceeds 50%, and it appears to have a positive correlation with the missing rate. For stations with higher missing data rates, particularly those with constructive missing data, such as SHAO, TASH, YONG, and ZHNZ, the degree of rank deficiency exceeds 90%. This means that when estimating $\boldsymbol{x}_2$, less than 10% of the valid components in $\boldsymbol{B}_2$ effectively contribute to parameter estimation, while the rest are treated as disturbances and discarded.

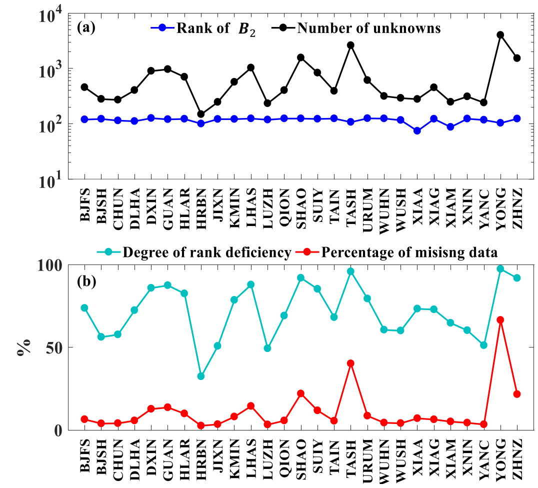

Fig. 7. (a) Rank of $\boldsymbol{B}_2$ and the number of unknowns N_S. (b) Degree of rank deficiency and percentage of missing data.

To quantitatively compare the two approaches, we calculate the fitting errors of the extracted signals using (30) and the signal-to-noise ratio (SNR) using (31)

$$\hat{\sigma} = \sqrt{\frac{1}{N_S}\sum_{i\in S}(x_i - s_i)^2} \tag{30}$$

$$\hat{r} = \sum_{i\in S} s_i^2 \Big/ \sum_{i\in S}(x_i - s_i)^2 . \tag{31}$$

Table I presents the fitting errors and SNRs for 27 stations using both methods. The results show that the MWF method produces smaller fitting errors and higher SNRs compared to the EWF method at all stations, indicating that it extracts more signals. We also apply the weighted EWF and MWF methods by considering the formal errors. Since Ji et al. [1] demonstrated that the iterative weighting scheme (the first scheme) outperforms the direct weighting in the cost function (the second scheme) for the EWF method, we only compare the weighted MWF method with the weighted EWF method using the iterative weighting scheme. Considering the formal errors, we calculate the weighted fitting errors of the extracted signals using (32) and the SNR values using (33)

$$\hat{\sigma}_w = \sqrt{\frac{1}{N_S}\sum_{i\in S}\frac{\sigma_0^2}{\sigma_i^2}(x_i - s_i)^2} \tag{32}$$

$$\hat{r}_w = \sum_{i\in S} s_i^2 \Big/ \sum_{i\in S}\frac{\sigma_0^2}{\sigma_i^2}(x_i - s_i)^2 . \tag{33}$$

TABLE I
FITTING ERRORS AND SNR VALUES OF 27 STATIONS. EWF (W) AND MWF (W) MEAN-WEIGHTED EWF AND MWF METHODS

	Fitting errors (mm)				SNR values			
	EWF	MWF	EWF(W)	MWF(W)	EWF	MWF	EWF(W)	MWF(W)
BJFS	3.7809	**3.7724**	3.1765	**3.1665**	2.6442	**2.6636**	3.7389	**3.7686**
BJSH	3.8925	**3.8800**	3.6693	**3.6561**	1.3529	**1.3686**	1.5177	**1.5356**
CHUN	4.4708	**4.4243**	4.3169	**4.2706**	2.6710	**2.7519**	2.8501	**2.9366**
DLHA	2.5170	**2.5110**	2.0517	**2.0472**	3.2208	**3.2425**	4.8430	**4.8703**
DXIN	3.0091	**2.9853**	2.8618	**2.8470**	1.6530	**1.6967**	1.8263	**1.8678**
GUAN	6.2061	**6.1837**	5.0544	**5.0298**	1.6248	**1.6433**	2.4516	**2.4731**
HLAR	4.2854	**4.2598**	4.1591	**4.1293**	8.2937	**8.4102**	8.7776	**8.9195**
HRBN	4.0483	**4.0169**	3.8873	**3.8548**	1.2923	**1.3332**	1.3978	**1.4426**
JIXN	3.5946	**3.5811**	3.3759	**3.3634**	1.8772	**1.9020**	2.1238	**2.1503**
KMIN	5.1143	**5.1020**	4.9842	**4.9653**	3.6307	**3.6489**	3.8187	**3.8485**
LHAS	3.7676	**3.7409**	3.5885	**3.5617**	2.8530	**2.9089**	3.1405	**3.2039**
LUZH	4.0104	**4.0087**	3.8757	**3.8735**	1.5390	**1.5412**	1.6454	**1.6476**
QION	6.5916	**6.5524**	6.1570	**6.1278**	0.7646	**0.7864**	0.8738	**0.8978**
SHAO	4.1974	**4.1730**	3.4553	**3.4289**	1.9766	**2.0145**	2.9049	**2.9671**
SUIY	4.9185	**4.8839**	4.5865	**4.5594**	2.8701	**2.9302**	3.2947	**3.3532**
TAIN	4.4996	**4.4799**	4.1776	**4.1612**	1.7660	**1.7909**	2.0434	**2.0700**
TASH	3.7344	**3.7084**	3.4789	**3.4501**	1.8494	**1.8884**	2.1291	**2.1795**
URUM	4.2346	**4.1344**	4.1561	**3.9613**	3.1763	**3.3886**	3.2787	**3.6709**
WUHN	4.7053	**4.6903**	4.1515	**4.1380**	3.2529	**3.2798**	4.1676	**4.2001**
WUSH	3.8083	**3.7855**	3.6147	**3.5969**	2.4307	**2.4735**	2.6955	**2.7362**
XIAA	4.2456	**4.2214**	4.0461	**4.0227**	2.4773	**2.5129**	2.7212	**2.7608**
XIAG	6.6232	**6.6086**	6.1680	**6.1541**	1.8216	**1.8331**	2.0942	**2.1073**
XIAM	5.4390	**5.3792**	5.1410	**5.0735**	0.8095	**0.8494**	0.9030	**0.9520**
XNIN	2.8771	**2.8674**	2.7443	**2.7366**	3.3324	**3.3633**	3.6585	**3.6893**
YANC	3.0947	**3.0822**	2.6084	**2.6024**	2.1085	**2.1342**	2.9641	**2.9897**
YONG	6.8743	**6.7688**	6.6899	**6.5736**	1.7379	**1.8259**	1.8322	**1.9334**
ZHNZ	4.1716	**4.1656**	3.9167	**3.9091**	3.1086	**3.1230**	3.4985	**3.5186**

The results, shown in Table I, indicate that considering formal errors effectively reduces the fitting errors and increases the SNR values for both two methods. However, the weighted MWF method still outperforms the weighted EWF method, which coincides with the theoretical analysis in Section II-C.

C. Synthetic Time-Series Analysis

To further demonstrate the performance of the proposed method, we conduct simulation experiments. In each simulation, the signals extracted from real data are regarded as true signals $\bar{s}$. We then generate random noise $\boldsymbol{e}$ and add it to $\bar{s}$ to obtain a noisy time series. Since true signals are available in simulations, we can directly compute the root-mean-square errors (RMSEs) of the extracted signals using the following equation:

$$\mathrm{RMSE} = \sqrt{\frac{1}{N_S}\sum_{i\in S}(\hat{s}_i - \bar{s}_i)^2}. \tag{34}$$

The locations of missing data are inherited from the real data. Initially, the noise is assumed to be normally distributed with zero mean and variance $\hat{\sigma}^2$, where $\hat{\sigma}$ is computed with (30). To assess the statistical performance, we repeat the simulations 50 times. Fig. 8 presents the RMSE values of the signals extracted by the two approaches for 50 simulations. The results clearly demonstrate that the signals extracted by the MWF method are closer to the simulated true signals compared to the EWF method for all 27 stations. We also compute the relative improvement with the following equation:

$$\mathrm{Imp1} = \frac{\overline{\mathrm{RMSE}}_{\mathrm{EWF}} - \overline{\mathrm{RMSE}}_{\mathrm{MWF}}}{\overline{\mathrm{RMSE}}_{\mathrm{EWF}}} \times 100\% \tag{35}$$

where $\overline{\mathrm{RMSE}}_{\mathrm{EWF}}$ and $\overline{\mathrm{RMSE}}_{\mathrm{MWF}}$ represent the average RMSE values for EWF and MWF, respectively. The results are shown in the unweighted case panel of Table II, with a maximum improvement is 39.2% in the URUM station and a mean of 12.8%.

To compare the MWF and EWF methods under heterogeneous data, we simulate noise with zero mean and a diagonal variance matrix with the formal errors inherited from the real data. Since the comparison between the EWF and MWF

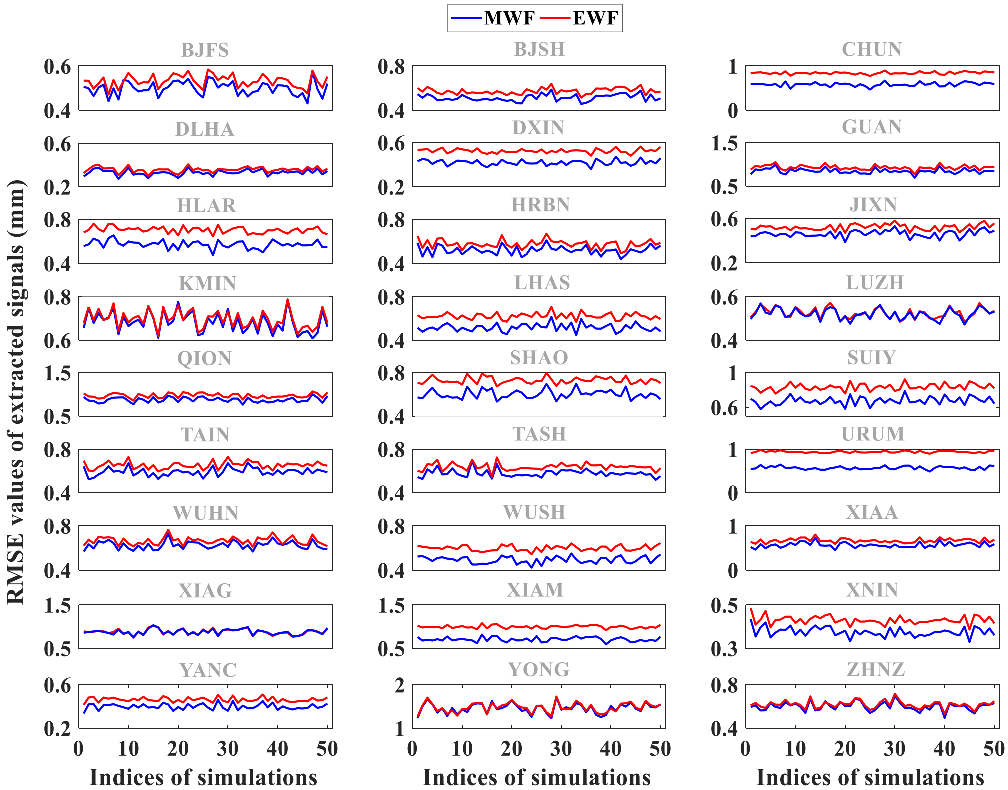

Fig. 8. RMSE values of signals extracted by the EWF and MWF methods across 50 simulations at 27 stations.

methods remains the same as the unweighted case, we do not present it for the weighted case. Fig. 9 shows the RMSE values for the unweighted EWF and weighted EWF methods, and Fig. 10 shows the RMSE values for the unweighted MWF and weighted MWF methods. The results indicate that the performance of both the EWF and MWF methods improves when considering formal errors. To quantify these improvements, we calculate the relative improvements with the following equations:

$$\text{Imp2} = \frac{\overline{\text{RMSE}}_{\text{EWF}} - \overline{\text{RMSE}}_{\text{WEWF}}}{\overline{\text{RMSE}}_{\text{EWF}}} \times 100\% \quad (36)$$

$$\text{Imp3} = \frac{\overline{\text{RMSE}}_{\text{MWF}} - \overline{\text{RMSE}}_{\text{WMWF}}}{\overline{\text{RMSE}}_{\text{MWF}}} \times 100\% \quad (37)$$

where $\overline{\text{RMSE}}_{\text{WEWF}}$ and $\overline{\text{RMSE}}_{\text{WMWF}}$ represent the average RMSE values for the weighted EWF and weighted MWF methods, respectively. The results are shown in the weighted case panel of Table II. It is clear that the weighting scheme proposed for the MWF method is superior to the one in the EWF method, which aligns with the theoretical analysis in Section II-C. Finally, we present a comparison of the weighted EWF and weighted MWF methods in Fig. 11, and compute the relative improvement

$$\text{Imp4} = \frac{\overline{\text{RMSE}}_{\text{WEWF}} - \overline{\text{RMSE}}_{\text{WMWF}}}{\overline{\text{RMSE}}_{\text{WEWF}}} \times 100\%. \quad (38)$$

The results show that the MWF method still outperforms the EWF method, even when formal errors are considered.

To investigate how the percentage of missing data affects signal extraction, we conduct repeated simulations with varying percentages of missing data, ranging from 10% to 60% in increments of 10%. Missing epochs are determined using two distribution types: uniform and consecutive distributions. For uniform missing data, we use the MATLAB built-in function “randi” to randomly select missing epochs. For consecutive missing data, we start from the 2000th epoch and generate a continuous set of integers based on the specified missing percentage to represent the missing epochs. Figs. 12 and 13 show the RMSE values of the extracted signals for different percentages of missing data under both distribution types. The results indicate that the MWF method consistently outperforms the EWF method, regardless of whether the gaps are uniformly or consecutively distributed. Table III provides the average RMSE values across 50 simulations.

As the percentage of missing data increases, the relative improvement of the MWF method over the EWF method decreases for the case of uniform data gaps but increases for the case of consecutive data gaps. To explore this difference, we conduct a simulation with 20% missing data, using both uniform and consecutive gaps. Fig. 14 shows the comparison of the simulated true signals with the extracted signals at observed and missing epochs. The results indicate that the extracted signals at observed epochs are very close to the true signals for both gap distribution types, suggesting that filtering works well, even with consecutive data gaps. However, for missing epochs, the extracted signals are acceptable for uniform data gaps but highly unreliable for consecutive gaps. Recalling that the core criterion of the EWF method depends on stable residual estimates at both observed and missing epochs [see (19)]. In contrast, our MWF method only considers minimizing the residuals at the observed epochs,

TABLE II
AVERAGE RMSE VALUES OF EWF AND MWF METHODS FOR THE UNWEIGHTED AND WEIGHTED CASES AND SEVERAL RELATIVE IMPROVEMENTS

	Unweighted case			Weighted case						
	EWF (mm)	MWF (mm)	**Imp1 (%)**	EWF (mm)	MWF (mm)	EWF(W) (mm)	MWF(W) (mm)	**Imp2 (%)**	**Imp3 (%)**	**Imp4 (%)**
BJFS	0.5319	0.4987	**6.2**	0.7032	0.6855	0.6862	0.6505	**2.4**	**5.1**	**5.2**
BJSH	0.5728	0.5137	**10.3**	0.8718	0.8429	0.8318	0.7916	**4.6**	**6.1**	**4.8**
CHUN	0.8401	0.5828	**30.6**	1.3743	1.26	1.3509	1.2245	**1.7**	**2.8**	**9.4**
DLHA	0.3589	0.3325	**7.4**	0.6131	0.6146	0.6089	0.6080	**0.7**	**1.1**	**0.1**
DXIN	0.525	0.4206	**19.9**	1.0689	1.0571	1.0535	1.0371	**1.4**	**1.9**	**1.6**
GUAN	0.9282	0.8457	**8.9**	1.6357	1.6009	1.6118	1.5551	**1.5**	**2.9**	**3.5**
HLAR	0.7033	0.5725	**18.6**	1.135	1.0749	1.1049	1.0312	**2.7**	**4.1**	**6.7**
HRBN	0.5766	0.5211	**9.6**	0.9137	0.8915	0.8902	0.855	**2.6**	**4.1**	**4**
JIXN	0.5217	0.4616	**11.5**	0.8967	0.8714	0.8616	0.8298	**3.9**	**4.8**	**3.7**
KMIN	0.697	0.6827	**2.1**	1.7369	1.747	1.7305	1.7231	**0.4**	**1.4**	**0.4**
LHAS	0.6214	0.5164	**16.9**	1.1163	1.0958	1.0962	1.0714	**1.8**	**2.2**	**2.3**
LUZH	0.5248	0.5206	**0.8**	1.1059	1.123	1.0803	1.0977	**2.3**	**2.3**	**-1.6**
QION	0.9714	0.8742	**10**	1.6763	1.6923	1.6350	1.6244	**2.5**	**4**	**0.6**
SHAO	0.7286	0.6013	**17.5**	1.1129	1.0421	1.0882	0.9892	**2.2**	**5.1**	**9.1**
SUIY	0.8331	0.6756	**18.9**	1.1194	1.0195	1.1116	0.9914	**0.7**	**2.8**	**10.8**
TAIN	0.653	0.5929	**9.2**	1.1697	1.1652	1.121	1.1083	**4.2**	**4.9**	**1.1**
TASH	0.6377	0.5785	**9.3**	1.2253	1.21	1.2096	1.1857	**1.3**	**2**	**2**
URUM	0.9387	0.5706	**39.2**	1.0169	0.6997	0.9951	0.6590	**2.1**	**5.8**	**33.8**
WUHN	0.6654	0.6256	**6**	0.9022	0.882	0.8745	0.8403	**3.1**	**4.7**	**3.9**
WUSH	0.5989	0.493	**17.7**	1.144	1.1191	1.1288	1.101	**1.3**	**1.6**	**2.5**
XIAA	0.6678	0.5667	**15.1**	1.0129	0.9723	0.9847	0.9413	**2.8**	**3.2**	**4.4**
XIAG	0.8812	0.8787	**0.3**	1.3497	1.3656	1.3076	1.32	**3.1**	**3.3**	**-0.9**
XIAM	0.996	0.7083	**28.9**	1.5272	1.4084	1.5029	1.3704	**1.6**	**2.7**	**8.8**
XNIN	0.4302	0.3762	**12.6**	0.814	0.8092	0.7973	0.7893	**2.1**	**2.5**	**1**
YANC	0.4626	0.3985	**13.9**	0.7157	0.6884	0.7115	0.6852	**0.6**	**0.5**	**3.7**
YONG	1.4788	1.4592	**1.3**	3.6793	3.6153	3.655	3.5666	**0.7**	**1.3**	**2.4**
ZHNZ	0.6184	0.601	**2.8**	1.0773	1.0853	1.0207	1.0148	**5.3**	**6.5**	**0.6**

which remain stable even with consecutive missing data. As a result, the advantage of the MWF method over the EWF method becomes more apparent as the percentage of missing data increases for consecutive gaps.

For the case of uniform data gaps, surrounding observations anchor the gaps, making the second constraint term $\boldsymbol{e}_2^{\mathrm{T}}\boldsymbol{e}_2$ in (19) more reliable than in the case of constructive gaps. This acts as an effective constraint to address the rank deficiency of the model established with the criterion min: $\boldsymbol{e}_1^{\mathrm{T}}\boldsymbol{e}_1$, which is similar to, but distinct from, the minimum norm constraint of $\boldsymbol{x}_2$ used in the MWF method. Even with a high missing rate (e.g., 60%), the extracted signals at missing epochs remain reliable, as shown in Fig. 15, with RMSE values for both observed and missing epochs provided. Therefore, the improvement of the MWF method over the EWF method decreases as the percentage of missing data increases for uniform data gaps. Nevertheless, the signal estimates at observed epochs are always more reliable than those at missing epochs (see the RMSE values labeled on the chart), which passes down to the residuals and partly explains the superiority of the MWF method over the EWF method. Additionally, Fig. 14 shows that for the case of uniform gaps, the MWF method reduces the bias at the endpoints of the time series compared to the EWF method. For the case of consecutive gaps, the MWF method reduces the bias at the endpoints of those gaps.

To further compare EWF and MWF, we adopted the simulation strategy of Klos et al. [72], which is based on the trajectory model. Specifically, 500 synthetic gap-free time series of length N days were generated. Each simulation was composed of pure flicker noise (spectral index κ of -1) with amplitudes of σ_f mm/year$^{0.25}$, to which annual and semiannual signals with amplitudes A_1 and A_2 mm were added. To mimic time-varying seasonality, the amplitudes of the seasonal signals were allowed to vary with standard deviations of θ_1 and θ_2 mm for the annual and semiannual components, respectively. The parameter σ_f was determined from real estimates

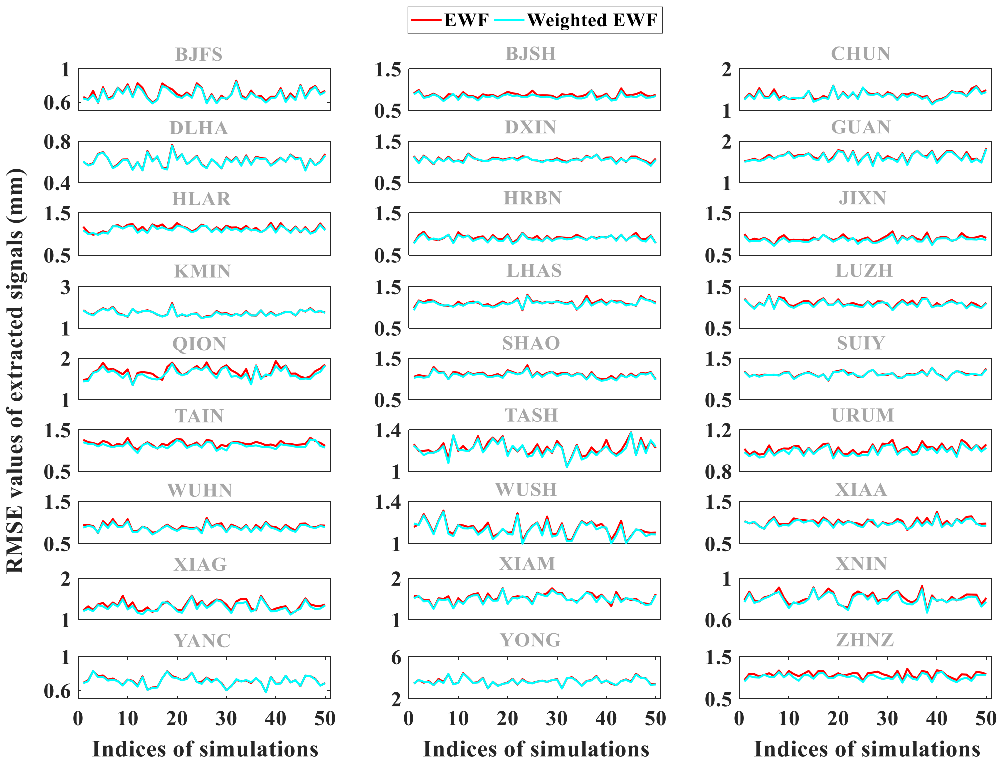

Fig. 9. RMSE values of signals extracted by the EWF and weighted EWF methods across 50 simulations at 27 stations.

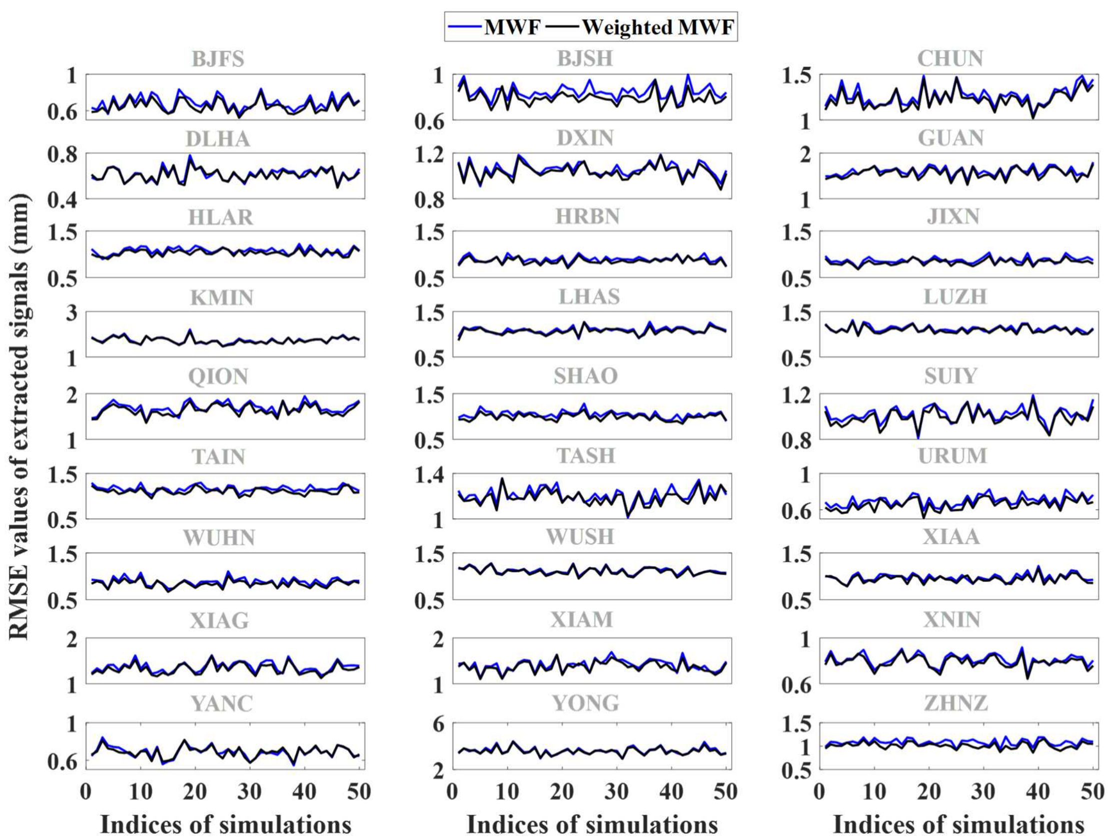

Fig. 10. RMSE values of signals extracted by the MWF and weighted MWF methods across 50 simulations at 27 stations.

(rounded down) at the BJFS and SHAO stations by assuming a white noise (WN) plus power-law noise (PLN) model using Hector software [25]. The value of N was taken as the full length of the BJFS and SHAO records, while the parameters

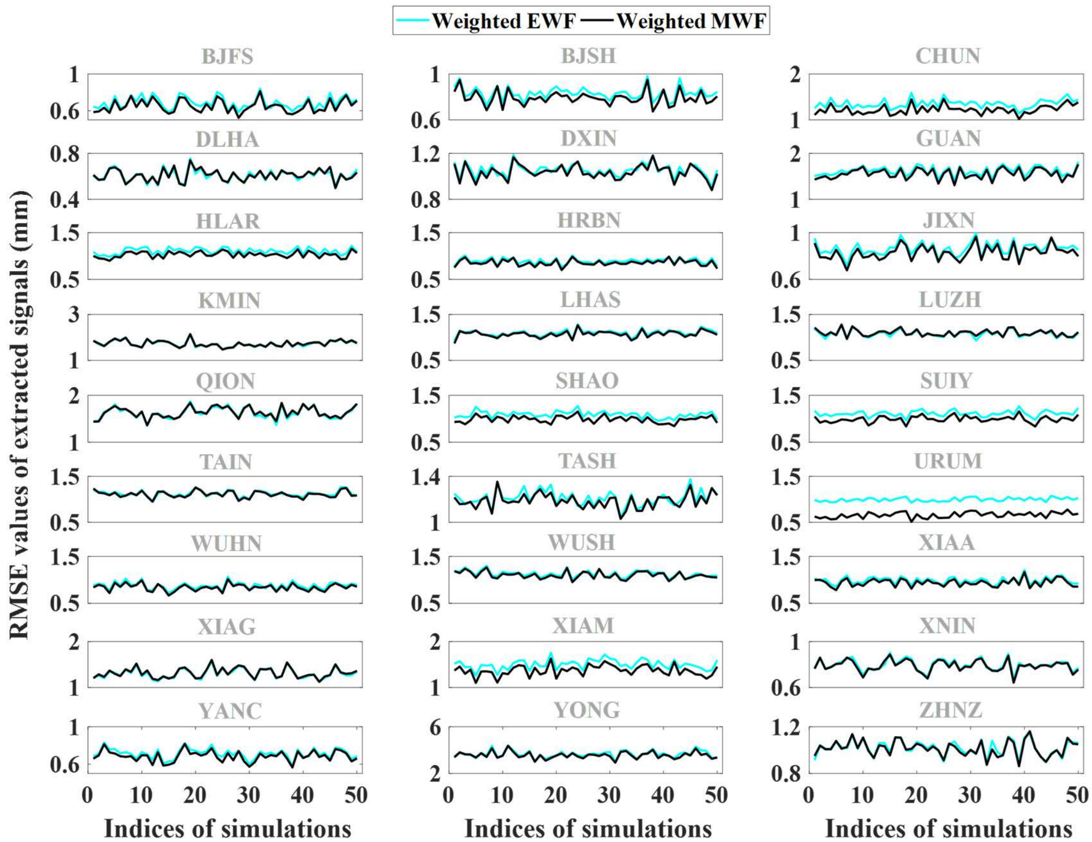

Fig. 11. RMSE values of signals extracted by the weighted EWF and weighted MWF methods across 50 simulations at 27 stations.

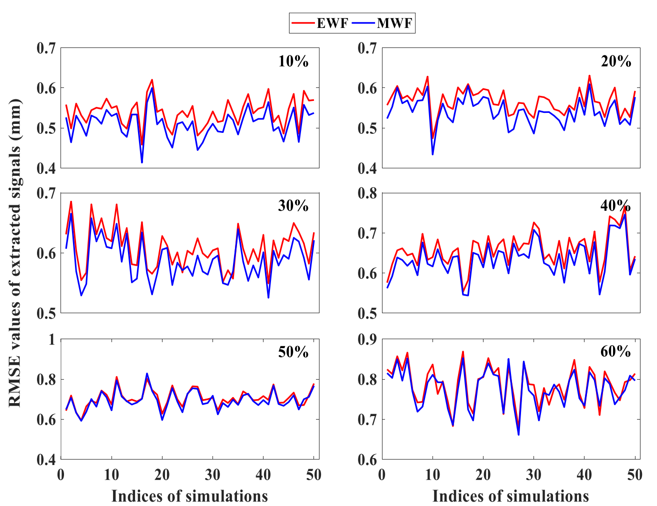

Fig. 12. RMSE values of signals extracted by the EWF and MWF methods across 50 simulations with varying percentages of missing data under uniformly distributed data gaps.

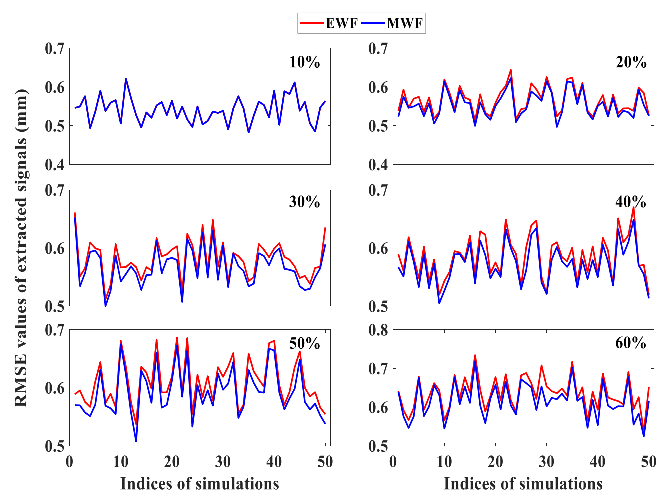

Fig. 13. RMSE values of signals extracted by the EWF and MWF methods across 50 simulations with varying percentages of missing data under consecutively distributed data.

of the annual and semiannual signals were determined from segmented time-series analyses (see [72] for details). We note that real GNSS position time series contain abundant periodic signals in addition to the annual and semiannual terms, such as draconitic and Chandler components and their harmonics [80]. In this study, however, the simulations only include the dominant annual and semiannual signals, which can be effectively captured by wavelet methods, in order to compare EWF and MWF.

Data gaps were then introduced by removing points according to the actual missing epochs in the BJFS and SHAO observations. Since the true signals were known, we directly computed the RMSEs of the signals estimated by the two methods. Table IV shows the mean RMSE values from 500 simulations, showing that MWF yields estimates closer to the true signals than EWF. After extracting seasonal signals using EWF and MWF, these components were removed from the synthetic series. The residuals were subsequently analyzed

TABLE III

AVERAGE RMSE VALUES OF THE TWO METHODS WITH VARYING PERCENTAGES OF MISSING DATA (MP) UNDER UNIFORM AND CONSECUTIVE DATA GAPS

	Uniform data gaps			Constructive data gaps		
MP	EWF	MWF	Imp	EWF	MWF	Imp
10%	0.5387	0.5111	5.12%	0.5414	0.5414	0
20%	0.5666	0.5423	4.29%	0.5654	0.5546	1.91%
30%	0.6081	0.5878	3.34%	0.5809	0.5677	2.27%
40%	0.6571	0.6354	3.30%	0.5852	0.5727	2.14%
50%	0.7051	0.6946	1.49%	0.6102	0.5930	2.82%
60%	0.7853	0.7764	1.13%	0.6357	0.6161	3.08%

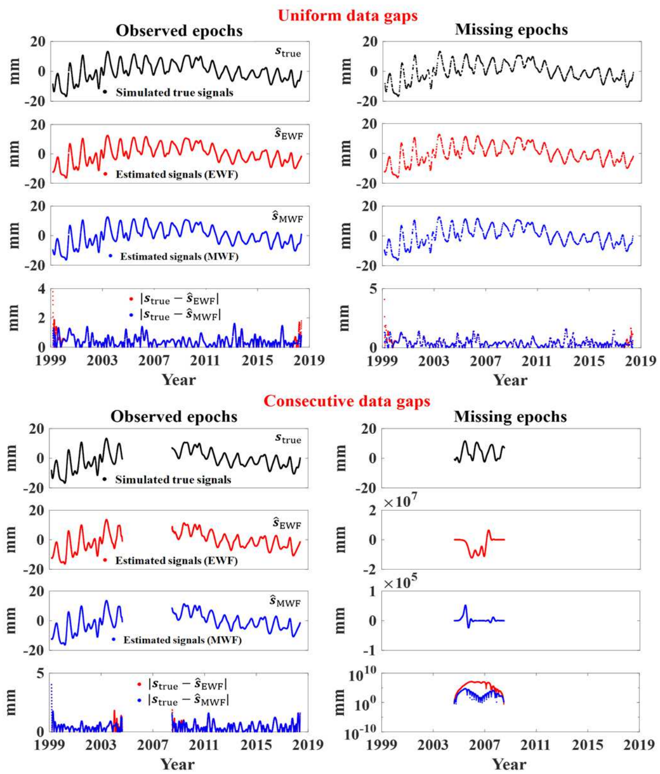

Fig. 14. Comparison of the simulated true signals and extracted signals at available and missing epochs under different distributions of data gaps.

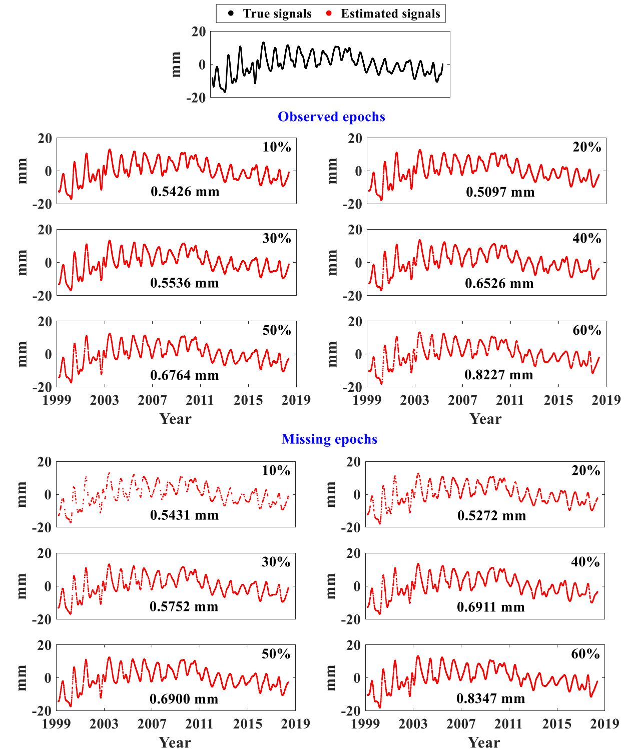

Fig. 15. Comparison of the simulated true signals and signals extracted by the EWF method with varying percentages of missing data.

TABLE IV

MEAN TU, SPECTRAL INDEX κ, NOISE AMPLITUDE σ_f, AND RMSE VALUES FROM 500 SIMULATIONS

BJFS $A_1 = 4.8, \theta_1 = 1.4, A_2 = 1.4, \theta_2 = 0.8, N = 7022$			
	EWF	MWF	Actual
TU (mm/year)	0.171	0.176	0.209
κ	-0.94	-0.95	-1.00
$\sigma(\mathrm{mm/year}^{-\kappa/4})$	10.29	10.37	11.00
RMSE (mm)	1.78	1.56	/
SHAO $A_1 = 3.7, \theta_1 = 2.2, A_2 = 1.5, \theta_2 = 0.9, N = 7082$			
	EWF	MWF	Actual
TU (mm/year)	0.145	0.153	0.188
κ	-0.92	-0.94	-1.00
$\sigma(\mathrm{mm/year}^{-\kappa/4})$	9.17	9.26	10.00
RMSE (mm)	1.65	1.28	/

with maximum likelihood estimation (MLE), assuming a WN plus PLN model, to estimate noise parameters (σ_f and κ) and trend uncertainty (TU). Table IV further lists the mean values of the estimated noise components, spectral index, and TU. The results indicate that the noise parameters obtained with MWF are more consistent with the true values than those from EWF.

IV. DISCUSSION

To further demonstrate the effectiveness of the proposed MWF method, we compare it with several alternative methods, including the following.

1) Iterative wavelet filtering (IWF), which performs CWF iteratively, filling the data gaps with values from missing epochs in the filtered signals from the previous iteration. The iteration stops when the threshold $\max(|\Delta s|) <$ 0.001 mm is reached, where Δs represents the difference between adjacent solutions.
2) CWF with the missing data filled using the extended SSA (ESSA) method [29] based on the optimal low-rank approximation in the temporal domain.
3) CWF with the missing data filled by the extended principal component analysis (EPCA) method [30] based on the optimal low-rank approximation in the spatiotemporal domain.

Table V presents the fitting errors of the signals extracted by different approaches and the SNR values for 27 stations, computed with (30) and (31). The results demonstrate that our MWF method also outperforms the IWF and CWF using interpolations. To further evaluate the performance of the

TABLE V

FITTING ERRORS AND SNR VALUES OF 27 STATIONS CWF (ESSA) AND CWF (EPCA) MEANS CWF METHOD USING ESSA AND EPCA INTERPOLATIONS

	Fitting errors (mm)					SNR values				
	MWF	IWF	CWF(ESSA)	CWF(EPCA)	LSFF	**MWF**	IWF	CWF(ESSA)	CWF(EPCA)	LSFF
BJFS	**3.7724**	3.7810	3.7825	3.8060	3.7954	**2.6636**	2.6443	2.6299	2.4296	2.6193
BJSH	**3.8800**	3.8926	3.8926	3.9035	3.8856	**1.3686**	1.3530	1.3499	1.2508	1.3618
CHUN	**4.4243**	4.4709	4.4714	4.5137	4.4643	**2.7519**	2.6706	2.6578	2.3175	2.6851
DLHA	**2.5110**	2.5170	2.5185	2.5523	2.5823	**3.2425**	3.2210	3.1979	2.8684	3.0092
DXIN	**2.9853**	3.0096	3.0113	3.0522	3.0417	**1.6967**	1.6519	1.6363	1.4135	1.5976
GUAN	**6.1837**	6.2061	6.2132	6.3333	6.1793	**1.6433**	1.6250	1.6098	1.3268	1.6471
HLAR	**4.2598**	4.2872	4.2948	4.4403	4.2985	**8.4102**	8.2876	8.2513	7.4122	8.2415
HRBN	**4.0169**	4.0490	4.0502	4.0747	4.0581	**1.3332**	1.2914	1.2884	1.1644	1.2861
JIXN	**3.5811**	3.5949	3.5948	3.606	3.5930	**1.9020**	1.8772	1.8741	1.7467	1.8827
KMIN	**5.1020**	5.1143	5.1161	5.2515	5.1703	**3.6489**	3.6310	3.6171	3.101	3.5269
LHAS	**3.7409**	3.7682	3.7768	4.0374	3.7727	**2.9089**	2.8508	2.8318	2.3164	2.8432
LUZH	**4.0087**	4.0104	4.0105	4.0232	4.0312	**1.5412**	1.5390	1.5368	1.4537	1.5130
QION	**6.5524**	6.5917	6.5926	6.636	6.5994	**0.7864**	0.7646	0.7613	0.6602	0.7611
SHAO	**4.1730**	4.2144	4.2184	4.2828	4.1775	**2.0145**	1.9523	1.9440	1.7412	2.0080
SUIY	**4.8839**	4.9281	4.9320	4.9669	4.9187	**2.9302**	2.8560	2.8468	2.7096	2.8748
TAIN	**4.4799**	4.4997	4.5014	4.5368	4.5037	**1.7909**	1.7655	1.7658	1.512	1.7616
TASH	**3.7084**	3.7597	3.7658	3.8532	3.7335	**1.8884**	1.8090	1.7946	1.533	1.8496
URUM	**4.1344**	4.2346	4.2371	4.4462	4.2179	**3.3886**	3.1758	3.1528	2.5492	3.2164
WUHN	**4.6903**	4.7053	4.7056	4.7374	4.7152	**3.2798**	3.2525	3.2464	2.969	3.2347
WUSH	**3.7855**	3.8085	3.8094	3.8326	3.9344	**2.4735**	2.4301	2.4161	2.229	2.2155
XIAA	**4.2214**	4.2457	4.2468	4.2965	4.3186	**2.5129**	2.4774	2.4674	2.1694	2.3566
XIAG	**6.6086**	6.6232	6.6235	6.6749	6.6915	**1.8331**	1.8217	1.8149	1.6516	1.7634
XIAM	**5.3792**	5.4393	5.4427	5.4747	5.4409	**0.8494**	0.8096	0.7984	0.7348	0.8076
XNIN	**2.8674**	2.8771	2.8775	2.897	2.9079	**3.3633**	3.3324	3.3294	3.0983	3.2426
YANC	**3.0822**	3.0948	3.0948	3.1276	3.1143	**2.1342**	2.1085	2.1014	1.8336	2.0699
YONG	**6.7688**	6.9552	6.9844	8.1475	6.7274	**1.8259**	1.6748	1.6124	0.5483	1.8608
ZHNZ	**4.1656**	4.1742	4.1802	4.2563	4.1990	**3.1230**	3.1018	3.0882	2.6659	3.0576

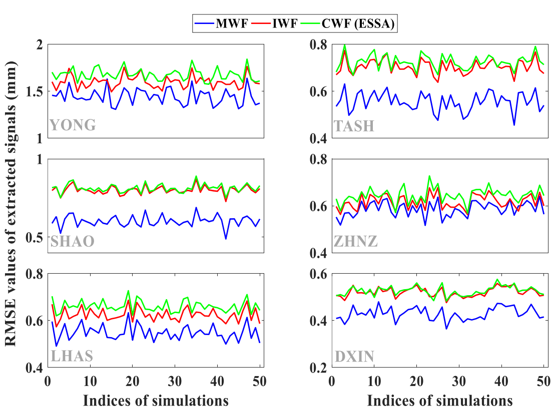

Fig. 16. RMSE values of the extracted signals by MWF, IWF, and CWF with ESSA interpolations.

proposed method, we conduct repeated simulations based on the stations with the top six highest missing data proportions: YONG, TASH, SHAO, ZHNZ, LHAS, and DXIN. Fig. 16 shows the RMSEs of the signals extracted by different methods across 50 simulations. The results demonstrate that the signals extracted by our MWF method are closer to the simulated true signals than the other two methods. We also compare MWF with the recently proposed LS Fourier filtering (LSFF) [81], which adopts a similar minimum weighted norm optimization framework as MWF, but in the frequency domain using trigonometric basis functions instead of wavelets. The fitting errors and SNR values for LSFF, also shown in Table V, confirm that MWF outperforms LSFF. This improvement is mainly attributed to: 1) the superior time–frequency localization properties of wavelet functions compared to trigonometric functions and 2) the updated minimum weighted norm least-squares criterion in MWF, which is applied only to available epochs, unlike LSFF, which applies the criterion to both available and missing epochs.

We would like to clarify that the superiority of the proposed MWF over EWF remains unchanged as the employed mother wavelet. We performed additional experiments to examine how different mother wavelets affect filtering performance. Specifically, we compared the proposed MWF and conven-

TABLE VI
FITTING ERRORS OF SIGNALS EXTRACTED BY EWF AND MWF, AND SNR VALUES USING db6 WAVELETS

	Fitting errors (mm)				SNR values			
	EWF	MWF	EWF(W)	**MWF(W)**	EWF	MWF	EWF(W)	**MWF(W)**
BJFS	3.7853	3.7792	3.1795	**3.1758**	2.6377	2.6504	3.7302	**3.7404**
BJSH	3.8748	3.8635	3.6608	**3.6508**	1.3782	1.3888	1.5398	**1.5504**
CHUN	4.4193	4.3775	4.2546	**4.2003**	2.7598	2.8327	2.9636	**3.0607**
DLHA	2.5474	2.5435	2.0595	**2.0582**	3.1139	3.126	4.7603	**4.77**
DXIN	2.9866	2.9718	2.8383	**2.8287**	1.6909	1.7212	1.8709	**1.8979**
GUAN	6.1809	6.1571	5.0253	**5.0008**	1.6512	1.6662	2.499	**2.5134**
HLAR	4.2701	4.2657	4.1383	**4.1342**	8.3638	8.3842	8.8773	**8.8968**
HRBN	4.0385	4.0218	3.8839	**3.8649**	1.3137	1.3276	1.4158	**1.4329**
JIXN	3.5825	3.5756	3.3701	**3.3648**	1.8998	1.911	2.1401	**2.1507**
KMIN	5.2248	5.2179	5.0916	**5.0808**	3.4395	3.4445	3.6158	**3.6261**
LHAS	3.8007	3.7731	3.6136	**3.5855**	2.7907	2.8424	3.0795	**3.1388**
LUZH	4.0231	4.0196	3.8964	**3.8928**	1.5201	1.5274	1.6179	**1.6257**
QION	6.6274	6.604	6.2024	**6.1857**	0.746	0.7586	0.8483	**0.8609**
SHAO	4.237	4.2177	3.5172	**3.5055**	1.9241	1.951	2.7813	**2.8106**
SUIY	4.9156	4.9043	4.5941	**4.5872**	2.8805	2.8975	3.2873	**3.3011**
TAIN	4.5069	4.4971	4.1951	**4.1859**	1.7604	1.7697	2.0254	**2.0357**
TASH	3.7929	3.773	3.5258	**3.5113**	1.7596	1.7903	2.0345	**2.0647**
URUM	4.2194	4.2029	4.1207	**4.1093**	3.2183	3.2466	3.3593	**3.3761**
WUHN	4.6822	4.6722	4.1383	**4.1285**	3.2935	3.3131	4.1951	**4.211**
WUSH	3.891	3.8866	3.6601	**3.6562**	2.2906	2.2951	2.5838	**2.5886**
XIAA	4.2981	4.2801	4.1118	**4.0936**	2.3986	2.4172	2.614	**2.636**
XIAG	6.64	6.6264	6.1917	**6.1781**	1.8055	1.8179	2.0694	**2.0839**
XIAM	5.43	5.3977	5.1354	**5.0912**	0.8135	0.8367	0.906	**0.9367**
XNIN	2.9266	2.9169	2.7915	**2.7846**	3.1908	3.2165	3.5021	**3.5243**
YANC	3.1139	3.1052	2.6233	**2.6206**	2.0717	2.088	2.9153	**2.9263**
YONG	6.7897	6.7114	6.6129	**6.5206**	1.8064	1.8744	1.9025	**1.9841**
ZHNZ	4.18	4.1745	3.9239	**3.9188**	3.0845	3.1054	3.4673	**3.4893**

tional EWF methods using two other commonly used wavelets: Daubechies-6 (db6) and discrete Meyer wavelet (dmey). The fitting errors and SNR values for 27 stations are reported in Tables VI and VII. The results confirm that MWF consistently extracts more signal than EWF, regardless of the chosen mother wavelet.

We also compare the computational efficiency of different methods. To ensure robust statistics, each experiment is repeated 50 times, and the average computation time across 27 stations was calculated, as shown in Fig. 17. The computation time is measured using MATLAB's built-in tic and toc functions. All computations were performed in MATLAB 2017 on a Windows 10 system with a 12th Gen Intel[1] Core[2] i7-12700 2.10-GHz processor and 32 GB of RAM. The results indicate that MWF and EWF have comparable computation times, both slightly higher than that of IWF. This is expected, as MWF and EWF require solving inverse problems, whereas IWF relies solely on forward modeling. Nevertheless, all methods demonstrate acceptable computation times. For most stations with time series longer than 20 years, MWF completes in less than 10 s.

[1]Registered trademark.
[2]Trademarked.

V. CONCLUSION

A novel method called the MWF method is developed to extract signals from gappy geophysical time series without the need for interpolation. The proposed method is an improved version of our previous work, the EWF method, with a key difference in the core criterion used for filtering observed data. Specifically, we establish an equation with unknown parameters for the missing data and estimate the signals by minimizing the quadratic norm of residuals across only the observed epochs. This contrasts with EWF, which minimizes residuals across both observed and missing epochs. Since the equation is rank-deficient, we introduce an additional constraint to minimize the L2-norm of the parameters. Thanks to this modified criterion, compared to the EWF method, the MWF method not only filters observed data more effectively

TABLE VII
FITTING ERRORS OF SIGNALS EXTRACTED BY EWF AND MWF, AND SNR VALUES USING DMEY WAVELETS

	Fitting errors (mm)				SNR values			
	EWF	MWF	EWF(W)	**MWF(W)**	EWF	MWF	EWF(W)	**MWF(W)**
BJFS	3.7818	3.761	3.177	3.1644	2.6458	2.6858	3.7398	3.7837
BJSH	3.8729	3.8452	3.6574	3.6339	1.3764	1.4117	1.5385	1.5775
CHUN	4.4235	4.3477	4.2619	4.1697	2.7485	2.8854	2.9449	3.1163
DLHA	2.5417	2.5193	2.0546	2.0488	3.1353	3.2121	4.7911	4.8481
DXIN	2.9967	2.9529	2.8486	2.8154	1.6667	1.7561	1.8443	1.9304
GUAN	6.1553	6.0963	5.0225	4.9733	1.6662	1.7196	2.4973	2.5698
HLAR	4.2908	4.2199	4.159	4.101	8.279	8.5891	8.7832	9.1074
HRBN	4.0368	3.976	3.8801	3.8122	1.3083	1.3815	1.4124	1.4951
JIXN	3.5902	3.5534	3.3776	3.3508	1.8854	1.9473	2.1251	2.1929
KMIN	5.1751	5.119	5.042	4.9806	3.5156	3.6179	3.697	3.8319
LHAS	3.784	3.7224	3.6055	3.5585	2.8182	2.9479	3.098	3.2282
LUZH	4.0072	3.9792	3.8814	3.8567	1.5415	1.579	1.6404	1.6775
QION	6.5953	6.5313	6.1618	6.1153	0.762	0.798	0.8699	0.9082
SHAO	4.1799	4.1197	3.4293	3.3894	2.0036	2.0931	2.9631	3.0827
SUIY	4.9026	4.8395	4.5845	4.541	2.9006	3.0026	3.3107	3.4034
TAIN	4.4995	4.4652	4.1864	4.1514	1.7657	1.8094	2.0327	2.0841
TASH	3.7529	3.6301	3.4927	3.3847	1.8161	2.0143	2.0952	2.3209
URUM	4.1958	4.0885	4.0903	3.9093	3.2693	3.4876	3.4096	3.7916
WUHN	4.6838	4.6339	4.1371	4.0643	3.2882	3.3846	4.1945	4.3771
WUSH	3.8669	3.8251	3.6459	3.6095	2.3268	2.402	2.6113	2.6924
XIAA	4.2805	4.1422	4.0895	3.9512	2.4173	2.6486	2.6415	2.9161
XIAG	6.6347	6.5658	6.1822	6.1072	1.8096	1.8702	2.0772	2.1536
XIAM	5.4284	5.3068	5.1288	5.0234	0.8158	0.9002	0.9107	1.0063
XNIN	2.9132	2.8732	2.7795	2.753	3.2278	3.3457	3.5401	3.6488
YANC	3.0984	3.0774	2.6155	2.6091	2.0981	2.144	2.9401	2.9795
YONG	6.7705	6.5057	6.6008	6.3531	1.8252	2.059	1.9181	2.1699
ZHNZ	4.1805	4.1328	3.9209	3.8704	3.0904	3.1887	3.4791	3.604

but also provides a more concise way to incorporate a prior covariance matrix of the observed data during filtering, if available. The effectiveness of the proposed method is validated using both real and synthetic time-series data. Results show that the MWF method outperforms the EWF, IWF, and CWF methods using interpolations in filtering observed data.

Despite these advantages, several limitations remain as follows.

1) The proposed MWF method does not directly handle time series containing offsets or abrupt jumps. Therefore, appropriate preprocessing steps such as outlier detection/removal and jump detection/correction are required.
2) The current framework is specifically designed for processing a single incomplete time series.
3) The time complexity of the proposed MWF method is higher than that of CWF, which is the tradeoff for achieving higher filtering accuracy.
4) Due to the wavelet filtering structure, MWF may retain more noise in the filtered signal compared to SSA.

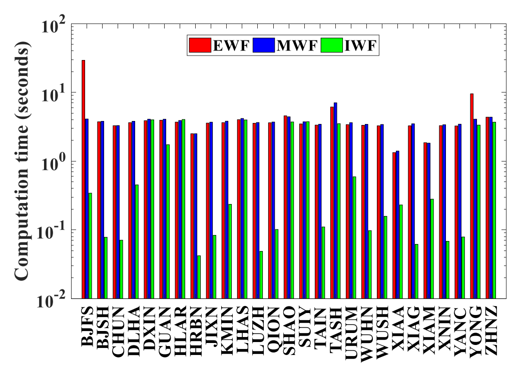

Fig. 17. Computation time of different methods.

To address these limitations, we plan the following future work.

1) Developing a robust version of MWF that is capable of handling outliers and jumps, for example, by replacing

Algorithm 1 DWT

Input: low-pass decomposition filter $\boldsymbol{h} \in \mathbb{R}^L$
high-pass decomposition filter $\boldsymbol{g} \in \mathbb{R}^L$
approximation coefficient $\boldsymbol{v}_{j-1} \in \mathbb{R}^{N_{j-1}}$
Output: approximation coefficient $\boldsymbol{v}_j \in \mathbb{R}^{N_j}$
detail coefficient $\boldsymbol{w}_j \in \mathbb{R}^{N_j}$
Note: $\left(N_j = \left[\left(N_{j-1} + L - 1\right)/2\right]\right)$
Begin
1) extending $\boldsymbol{v}_{j-1}$ as $\tilde{\boldsymbol{v}}_{j-1} \in \mathbb{R}^{N_{j-1}+2(L-1)}$ with: $\tilde{v}_{j-1,i} = \begin{cases} v_{j-1,L-i}, & 1 \le i < L \\ v_{j-1,i-L+1}, & L \le i < N_{j-1} + L \\ v_{j-1,2N_{j-1}+L-i}, & N_{j-1} + L \le i \le N_{j-1} + 2(L-1) \end{cases}$
2) convolve $\tilde{\boldsymbol{v}}_{j-1}$ with $\boldsymbol{h}$ and $\boldsymbol{g}$ to generate $\boldsymbol{c}_h$ and $\boldsymbol{c}_g$:
$c_{h,i} = \sum_{k=1}^{L} \tilde{v}_{j-1,k+i-1} h_{L+1-k}$
$c_{g,i} = \sum_{k=1}^{L} \tilde{v}_{j-1,k+i-1} g_{L+1-k} \left(1 \le i \le N_{j-1} + L - 1\right)$
3) downsampling
$v_{j,i} = c_{h,2i} \left(i = 1, 2, \ldots, N_j\right)$
$w_{j,i} = c_{g,2i} \left(i = 1, 2, \ldots, N_j\right)$
End

Algorithm 2 IDWT

Input: approximation coefficient $\boldsymbol{v}_j \in \mathbb{R}^{N_j}$
detail coefficient $\boldsymbol{w}_j \in \mathbb{R}^{N_j}$
low-pass reconstruction filter $\tilde{\boldsymbol{h}} \in \mathbb{R}^L$
high-pass reconstruction filter $\tilde{\boldsymbol{g}} \in \mathbb{R}^L$
Output: reconstructed coefficient $\boldsymbol{v}_{j-1} \in \mathbb{R}^{N_{j-1}}$
Note: $N_{j-1} = 2N_j - 2L + 2, kmin = \max(i - L + 1, 1), kmax = \min\left(i, 2N_j\right)$
Begin
1) upsampling $\boldsymbol{v}_j$ and $\boldsymbol{w}_j$ to generate $\boldsymbol{v}_j^{\uparrow} \in \mathbb{R}^{2N_j}$ and $\boldsymbol{w}_j^{\uparrow} \in \mathbb{R}^{2N_j}$
$v_{j,i}^{\uparrow} = \begin{cases} 0, & i = 1, 3, \ldots, 2N_j - 1 \\ v_{j,i/2}, & i = 2, 4, \ldots, 2N_j \end{cases}$
$w_{j,i}^{\uparrow} = \begin{cases} 0, & i = 1, 3, \ldots, 2N_j - 1 \\ w_{j,i/2}, & i = 2, 4, \ldots, 2N_j \end{cases}$
2) convolve $\boldsymbol{v}_j^{\uparrow}$ and $\boldsymbol{w}_j^{\uparrow}$ with $\tilde{\boldsymbol{h}}$ and $\tilde{\boldsymbol{g}}$ to generate $\tilde{\boldsymbol{c}}_h, \tilde{\boldsymbol{c}}_g \in \mathbb{R}^{2N_j+L-1}$
$\tilde{c}_{h,i} = \sum_{k=kmin}^{kmax} v_{j,k}^{\uparrow} \tilde{h}_{i-k+1}$
$\tilde{c}_{g,i} = \sum_{k=kmin}^{kmax} w_{j,k}^{\uparrow} \tilde{g}_{i-k+1}$
3) truncation
$v_{j-1,i} = \tilde{c}_{h,i+L-1} + \tilde{c}_{g,i+L-1} \left(1 \le i \le N_{j-1}\right)$
End

the L2-norm minimization with an L1-norm-based formulation.

2) Extending the MWF framework to multivariate and spatiotemporal settings by applying 2-D DWT and IDWT.
3) Exploring more efficient algorithms to solve the inverse problem more rapidly, particularly for large-scale applications.
4) Combine MWF with complementary signal decomposition or denoising techniques, such as SSA, to reduce residual noise and improve overall reconstruction quality.

Algorithm 3 Obtaining Projection Matrix $\boldsymbol{A}$

Input:
low-pass and high-pass filters: $\boldsymbol{h}, \boldsymbol{g}, \tilde{\boldsymbol{h}}, \tilde{\boldsymbol{g}} \in \mathbb{R}^L$
length of time series N
decomposition level J and reconstruction level r
Output:
projection matrix $\boldsymbol{A} \in \mathbb{R}^{N \times N}$
Begin
for $j = 1$ to N **do**
  $\boldsymbol{v}_0 = \boldsymbol{i}_j$
  for $k = 1$ to J
    obtaing $\boldsymbol{v}_k$ and $\boldsymbol{w}_k$ with $\boldsymbol{v}_{k-1}$ using Algorithm 1
  end
  Finally, we obtain $\boldsymbol{w}_k (1 \le k \le J)$ and $\boldsymbol{v}_J$
  setting $\boldsymbol{w}_i = \boldsymbol{0} (1 \le i \le r)$
  for $k = J$ to 1
    reconstructing $\boldsymbol{v}_{k-1}$ with $\boldsymbol{v}_k, \boldsymbol{w}_k$ using Algorithm 2
  end
  fill the jth column of $\boldsymbol{A}$ with $\boldsymbol{v}_0$
end
End

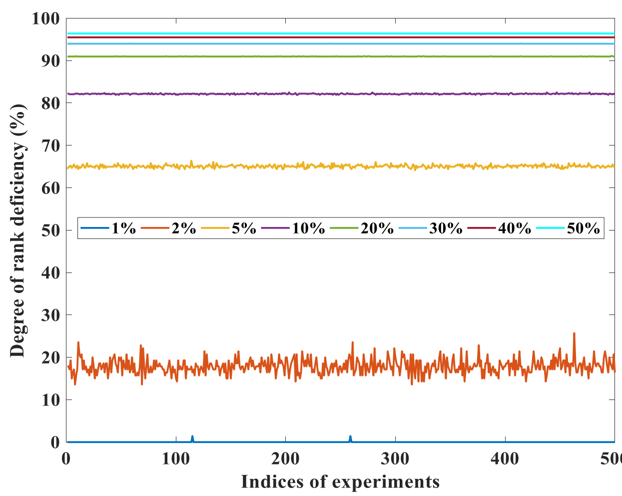

Fig. 18. Degree of rank deficiency under different percentages of missing data.

Appendix A

Algorithm 1 shows the flowchart for the single-level DWT, which consists of three steps.

1) Extend $\boldsymbol{v}_{j-1}$ to reduce border distortion. Here, we employ the symmetric padding mode, which is the default extension mode implemented in MATLAB. One can also use other modes, such as zero-padding and periodic padding. See [82] for details.
2) Convolve the extended time series $\tilde{\boldsymbol{v}}_{j-1}$ with the given decomposition filters $\boldsymbol{h}$ and $\boldsymbol{g}$ to obtain $\boldsymbol{c}_h$ and $\boldsymbol{c}_g$.
3) Downsample $\boldsymbol{c}_h$ and $\boldsymbol{c}_g$ to obtain $\boldsymbol{v}_j$ and $\boldsymbol{w}_j$. Algorithm 2 shows the flowchart for the single-level IDWT, which also consists of three steps: 1) upsample $\boldsymbol{v}_j$ and $\boldsymbol{w}_j$; 2) convolve the upsampled results with the given reconstruction filters $\tilde{\boldsymbol{h}}$ and $\tilde{\boldsymbol{g}}$; and 3) truncate the convolved results to obtain $\boldsymbol{v}_{j-1}$.

Algorithm 4 MWF Approach

Input:
incomplete time series $\boldsymbol{x}_1 \in \mathbb{R}^{N_S}$
its covariance matrix $\boldsymbol{\Sigma} \in \mathbb{R}^{N_S \times N_S}$ (optional)
index sets of missing epochs $\overline{S} \in \mathbb{R}^{N_{\overline{S}}}$
selected mother wavelet
decomposition level J and reconstruction level r
Output:
filtered signals $s_1 \in \mathbb{R}^{N_S}$
Begin
obtain projection matrix $\boldsymbol{A}$ via Algorithm 3
compute $\boldsymbol{B} = \boldsymbol{I}_N - \boldsymbol{A}$
obtain $\boldsymbol{A}_1, \boldsymbol{A}_2, \boldsymbol{B}_1, \boldsymbol{B}_2$ by subdividing $\boldsymbol{A}$ and $\boldsymbol{B}$
compute $\boldsymbol{y}_1 = \boldsymbol{B}_1 \boldsymbol{x}_1$
if $\boldsymbol{\Sigma}$ is available **then**
decompose $\boldsymbol{\Sigma}$ as $\boldsymbol{\Sigma} = \boldsymbol{L}\boldsymbol{L}^T$
update $\boldsymbol{B}_2$ with $\boldsymbol{L}^{-1}\boldsymbol{B}_2$ and $\boldsymbol{y}_1$ with $\boldsymbol{L}^{-1}\boldsymbol{y}_1$
end
decompose $\boldsymbol{B}_2$ as $\boldsymbol{B}_2 = \boldsymbol{U}\boldsymbol{\Lambda}\boldsymbol{V}^T = \sum_{i=1}^{N_{\overline{S}}} \lambda_i \boldsymbol{u}_i \boldsymbol{v}_i^T$
determine $r = \text{Rank}(\boldsymbol{B}_2) = \max(\{i \mid \lambda_i > \text{tor}\})$ with tor computed with Eq. (25);
compute $\boldsymbol{B}_2^+ = \sum_{i=1}^{r} 1/\lambda_i \boldsymbol{v}_i \boldsymbol{u}_i^T$
compute signals with $\boldsymbol{s}_1 = \left(\boldsymbol{A}_1 - \boldsymbol{A}_2 \boldsymbol{B}_2^+ \boldsymbol{B}_1\right)\boldsymbol{x}_1$
End

Appendix B

Algorithm 3 shows the flowchart for constructing matrix $\boldsymbol{A}$ using the Mallat pyramid algorithm. This process relies on multilevel DWT and IDWT, which involve repeatedly applying Algorithms 1 and 2.

Appendix C

Noting that $\boldsymbol{B}_2 = \boldsymbol{F}\boldsymbol{C}_2$, where $\boldsymbol{F}$ is a projection matrix with size $N_S \times N$, playing the role of transforming the complete time series to the observed data. The entries of $\boldsymbol{F}$ are given by

$$f_{ij} = \begin{cases} 1, & j = S(i) \\ 0, & \text{others} \end{cases} \tag{C1}$$

where $S(i)$ is the ith element of the index set of observed epochs S.

Since $\boldsymbol{B}_2$ has size $N_S \times N_{\overline{S}}$, its rank satisfies

$$\text{Rank}(\boldsymbol{B}_2) \le \min\left(N_S, N_{\overline{S}}\right). \tag{C2}$$

If $N_{\overline{S}} > N_S$, then

$$\text{Rank}(\boldsymbol{B}_2) \le N_S < N_{\overline{S}}. \tag{C3}$$

This means that when percentage of missing data exceeds 50%, $\boldsymbol{B}_2$ is column rank-deficient. For the case where $N_{\overline{S}} \le N_S$, i.e., the percentage of missing data does not exceed 50%, we have

$$\text{Rank}(\boldsymbol{B}_2) \le N_{\overline{S}}. \tag{C4}$$

It is challenging to determine whether equality holds, as this depends on the overlap between the row space of $\boldsymbol{F}$ and the column space of $\boldsymbol{C}_2$. The rank of a matrix represents the number of dimensions preserved in a linear mapping between the input and the output spaces. $\boldsymbol{F}$ essentially represents an isomorphism between a subspace $\mathbb{R}^{N_1}$ in the input space $\mathbb{R}^N$ and a subspace $\mathbb{R}^{N_S'}$ in the output space $\mathbb{R}^{N_S}$, and then, we have $\text{Rank}(\boldsymbol{F}) = \text{Dim}(\mathbb{R}^{N_1}) = \text{Dim}(\mathbb{R}^{N_S'}) = N_S$, where $\text{Dim}(\cdot)$ represents the operator to measure the dimension of a real space; similarly, $\boldsymbol{C}_2$ essentially represents an isomorphism between a subspace $\mathbb{R}^{N_{\overline{S}}'}$ in the input space $\mathbb{R}^{N_{\overline{S}}}$ and a subspace $\mathbb{R}^{N_2}$ and $\mathbb{R}^N$; thus, we have $\text{Rank}(C_2) = \text{Dim}(\mathbb{R}^{N_{\overline{S}}'}) = \text{Dim}(\mathbb{R}^{N_2}) = N_{\overline{S}}$.

When dealing with the composite mapping $\boldsymbol{F}\boldsymbol{C}_2$, the space $\mathbb{R}^N$ acts as a "bridge" for information transfer. Ideally, this bridge facilitates the greatest overlap between $\mathbb{R}^{N_1}$ and $\mathbb{R}^{N_2}$ (i.e., $\mathbb{R}^{N_1} \subseteq \mathbb{R}^{N_2}$ or $\mathbb{R}^{N_2} \subseteq \mathbb{R}^{N_1}$). This ensures that the information stored in $\mathbb{R}^{N_2}$ by $\boldsymbol{C}_2$ can be further transmitted through $\mathbb{R}^{N_1}$ by $\boldsymbol{F}$. In this ideal case, the rank of $\boldsymbol{F}\boldsymbol{C}_2$ is maximized: $\text{Rank}(\boldsymbol{F}\boldsymbol{C}_2) = \min(N_S, N_{\overline{S}})$. However, if there are dimensions in $\mathbb{R}^{N_1}$ and $\mathbb{R}^{N_2}$ that "do not overlap," the bridge $\mathbb{R}^N$ inevitably loses some information, causing $\boldsymbol{F}\boldsymbol{C}_2$ to be rank-deficient.

Clearly, if $N_{\overline{S}} > N_S$, then $\text{Dim}(\mathbb{R}^{N_2}) > \text{Dim}(\mathbb{R}^{N_1})$, indicating that $\mathbb{R}^{N_1}$ and $\mathbb{R}^{N_2}$ cannot fully overlap, leading to a rank deficiency in $\boldsymbol{F}\boldsymbol{C}_2$. Only when $N_{\overline{S}} \le N_S$ do, $\mathbb{R}^{N_1}$ and $\mathbb{R}^{N_2}$ have the potential to overlap. The smaller the $N_{\overline{S}}$, the higher the likelihood that $N_{\overline{S}}$. In this case, $\boldsymbol{F}\boldsymbol{C}_2$ achieves full rank, i.e., $\text{Rank}(\boldsymbol{F}\boldsymbol{C}_2) = \min(N_S, N_{\overline{S}}) = N_{\overline{S}}$. This scenario is more likely when the percentage of missing data is low. For example, if only one epoch is missing ($N_{\overline{S}} = 1$), based on (C4), we conclude that $\text{Rank}(\boldsymbol{B}_2) \le 1 = 1$, indicating that $\boldsymbol{B}_2$ is full column rank. To illustrate this, we design the experiments. Fig. 18 presents the degree of rank deficiency under different percentages of missing data: 1%, 2%, 5%, 10%, 20%, 30%, 40%, and 50%. For each scenario, the experiments are repeated 500 times. The results show that $\boldsymbol{B}_2$ achieves full column rank only when the missing rate is relatively very low, such as 1%. In other cases, $\boldsymbol{B}_2$ is rank-deficient, and the degree of rank deficiency increases as the missing rate rises.

Appendix D

Algorithm 4 gives the flowchart of the proposed MWF method.

References

[1] K. Ji, Y. Shen, F. Wang, Q. Chen, and L. Zhang, "Extended multiresolution analysis for filtering incomplete heterogeneous geophysical time series," *IEEE Trans. Geosci. Remote Sens.*, vol. 62, 2024, Art. no. 5921013.

[2] Y. Zhong and X. Chen, "Twofold subspace-based optimization method for solving inverse scattering problems," *Inverse Problems*, vol. 25, no. 8, Aug. 2009, Art. no. 085003.

[3] Y. Chen, X. Chen, Y. Wang, and S. Zu, "The interpolation of sparse geophysical data," *Surv. Geophys.*, vol. 40, no. 1, pp. 73–105, Sep. 2018.

[4] Y. Chen et al., "Simultaneous denoising and reconstruction of 5-D seismic data via damped rank-reduction method," *Geophys. J. Int.*, vol. 206, no. 3, pp. 1695–1717, Sep. 2016.

[5] B. D. Tapley, S. Bettadpur, J. C. Ries, P. F. Thompson, and M. M. Watkins, "GRACE measurements of mass variability in the Earth system," *Science*, vol. 305, no. 5683, pp. 503–505, Jul. 2004.

[6] X. Su et al., "High-resolution interannual mass anomalies of the Antarctic ice sheet by combining GRACE gravimetry and ENVISAT altimetry," *IEEE Trans. Geosci. Remote Sens.*, vol. 56, no. 1, pp. 539–546, Jan. 2018.

[7] Z. Shi et al., "Improving the spatial resolution of GRACE-derived ice sheet mass change in Antarctica," *IEEE Trans. Geosci. Remote Sens.*, vol. 63, 2025, Art. no. 4300112.

[8] X. Li, B. Zhong, J. Li, and H. Wang, "Investigating terrestrial water storage changes and their driving factors in the Southwest tiver basin of China using geodetic data," *IEEE Trans. Geosci. Remote Sens.*, vol. 61, 2023, Art. no. 5922115.

[9] S. Gu et al., "A fast generative adversarial network combined with transformer for downscaling GRACE terrestrial water storage data in Southwestern China," *IEEE Trans. Geosci. Remote Sens.*, vol. 62, 2024, Art. no. 4201616.

[10] Z. Jiang, Y.-J. Hsu, L. Yuan, and D. Huang, "Monitoring time-varying terrestrial water storage changes using daily GNSS measurements in yunnan, Southwest China," *Remote Sens. Environ.*, vol. 254, Mar. 2021, Art. no. 112249.

[11] A. Klos et al., "Introducing the idea of classifying sets of permanent GNSS stations as benchmarks for hydrogeodesy," *J. Geophys. Res., Solid Earth*, vol. 128, no. 9, Sep. 2023, Art. no. e2023JB026988.

[12] K. Yu, W. Ban, X. Zhang, and X. Yu, "Snow depth estimation based on multipath phase combination of GPS triple-frequency signals," *IEEE Trans. Geosci. Remote Sens.*, vol. 53, no. 9, pp. 5100–5109, Sep. 2015.

[13] S. Tabibi, F. Geremia-Nievinski, and T. van Dam, "Statistical comparison and combination of GPS, GLONASS, and multi-GNSS multipath reflectometry applied to snow depth retrieval," *IEEE Trans. Geosci. Remote Sens.*, vol. 55, no. 7, pp. 3773–3785, Jul. 2017.

[14] Y. Hu, X. Yuan, W. Liu, J. Wickert, and Z. Jiang, "GNSS-R snow depth inversion based on variational mode decomposition with multi-GNSS constellations," *IEEE Trans. Geosci. Remote Sens.*, vol. 60, 2022, Art. no. 2005512.

[15] J.-P. Montillet and K. Yu, "Modeling geodetic processes with levy α-Stable distribution and FARIMA," *Math. Geosci.*, vol. 47, no. 6, pp. 627–646, Aug. 2015.

[16] A. Klos, M. S. Bos, R. M. S. Fernandes, and J. Bogusz, "Noise-dependent adaption of the Wiener filter for the GPS position time series," *Math. Geosci.*, vol. 51, no. 1, pp. 53–73, Jan. 2019.

[17] D. F. Argus, W. R. Peltier, R. Drummond, and A. W. Moore, "The Antarctica component of postglacial rebound model ICE-6G_C (VM5a) based on GPS positioning, exposure age dating of ice thicknesses, and relative sea level histories," *Geophys. J. Int.*, vol. 198, no. 1, pp. 537–563, May 2014.

[18] J. Bogusz, A. Klos, and K. Pokonieczny, "Optimal strategy of a GPS position time series analysis for post-glacial rebound investigation in Europe," *Remote Sens.*, vol. 11, no. 10, p. 1209, May 2019.

[19] J. Montillet, T. I. Melbourne, and W. Szeliga, "GPS vertical land motion corrections to sea-level rise estimates in the Pacific Northwest," *J. Geophys. Res. Oceans*, vol. 123, no. 2, pp. 1196–1212, 2018.

[20] A. Klos, J. Kusche, L. Fenoglio-Marc, M. S. Bos, and J. Bogusz, "Introducing a vertical land motion model for improving estimates of sea level rates derived from tide gauge records affected by earthquakes," *GPS Solut.*, vol. 23, no. 4, 2019, Art. no. 102.

[21] K. Chanard, L. Fleitout, E. Calais, P. Rebischung, and J.-P. Avouac, "Toward a global horizontal and vertical elastic load deformation model derived from GRACE and GNSS station position time series," *J. Geophys. Res., Solid Earth*, vol. 123, no. 4, pp. 3225–3237, Apr. 2018.

[22] Z. Li, W. Chen, T. van Dam, P. Rebischung, and Z. Altamimi, "Comparative analysis of different atmospheric surface pressure models and their impacts on daily ITRF2014 GNSS residual time series," *J. Geodesy*, vol. 94, no. 4, pp. 1–20, Apr. 2020.

[23] A. Klos, H. Dobslaw, R. Dill, and J. Bogusz, "Identifying the sensitivity of GPS to non-tidal loadings at various time resolutions: Examining vertical displacements from continental Eurasia," *GPS Solutions*, vol. 25, no. 3, Jul. 2021, Art. no. 89.

[24] D. Dong et al., "Spatiotemporal filtering using principal component analysis and Karhunen–Loeve expansion approaches for regional GPS network analysis," *J. Geophys. Res., Solid Earth*, vol. 111, no. B3, pp. 3405–3421, Mar. 2006.

[25] M. S. Bos, R. M. S. Fernandes, S. D. P. Williams, and L. Bastos, "Fast error analysis of continuous GNSS observations with missing data," *J. Geodesy*, vol. 87, no. 4, pp. 351–360, Apr. 2013.

[26] J.-P. Montillet, P. Tregoning, S. McClusky, and K. Yu, "Extracting white noise statistics in GPS coordinate time series," *IEEE Geosci. Remote Sens. Lett.*, vol. 10, no. 3, pp. 563–567, May 2013.

[27] J.-P. Montillet, S. McClusky, and K. Yu, "Extracting colored noise statistics in time series via negentropy," *IEEE Signal Process. Lett.*, vol. 20, no. 9, pp. 857–860, Sep. 2013.

[28] A. Klos, M. A. Karegar, J. Kusche, and A. Springer, "Quantifying noise in daily GPS height time series: Harmonic function versus GRACE-assimilating modeling approaches," *IEEE Geosci. Remote Sens. Lett.*, vol. 18, no. 4, pp. 627–631, Apr. 2021.

[29] K. Ji, Y. Shen, Q. Chen, and F. Wang, "Extended singular spectrum analysis for processing incomplete heterogeneous geodetic time series," *J. Geodesy*, vol. 97, no. 8, Aug. 2023, Art. no. 74.

[30] K. Ji, Y. Shen, Q. Chen, and T. Feng, "Extended principal component analysis for spatiotemporal filtering of incomplete heterogeneous GNSS position time series," *IEEE Trans. Geosci. Remote Sens.*, vol. 61, 2023.

[31] A. Grinsted, J. C. Moore, and S. Jevrejeva, "Application of the cross wavelet transform and wavelet coherence to geophysical time series," *Nonlinear Processes Geophysics*, vol. 11, no. 5/6, pp. 561–566, Nov. 2004.

[32] M. J. A. Bolzan, A. M. S. Franco, and E. Echer, "A wavelet based method to remove the long term periodicities of geophysical time series," *Adv. Space Res.*, vol. 66, no. 2, pp. 299–306, Jul. 2020.

[33] D. Gabor, "Theory of communication. Part 1: The analysis of information," *J. Inst. Electr. Eng. III, Radio Commun. Eng.*, vol. 93, no. 26, pp. 429–441, Nov. 1946.

[34] J. P. Montillet et al., "Application of Lévy processes in modelling (geodetic) time series with mixed spectra," *Nonlinear Process. Geophys.*, vol. 28, no. 1, pp. 121–134, 2021.

[35] G. Kermarrec, F. Maddanu, A. Klos, T. Proietti, and J. Bogusz, "Modeling trends and periodic components in geodetic time series: A unified approach," *J. Geodesy*, vol. 98, no. 3, Mar. 2024, Art. no. 17.

[36] Q. Chen, T. van Dam, N. Sneeuw, X. Collilieux, M. Weigelt, and P. Rebischung, "Singular spectrum analysis for modeling seasonal signals from GPS time series," *J. Geodyn.*, vol. 72, pp. 25–35, Dec. 2013.

[37] K. Ji, Y. Shen, F. Wang, and Q. Chen, "An efficient improved singular spectrum analysis for processing GNSS position time series with missing data," *Geophys. J. Int.*, vol. 240, no. 1, pp. 189–200, Nov. 2024.

[38] W. Jiang, J. Wang, Z. Li, W. Li, and P. Yuan, "A new deep self-attention neural network for GNSS coordinate time series prediction," *GPS Solutions*, vol. 28, no. 1, Jan. 2024, Art. no. 3.

[39] J. L. Davis, B. P. Wernicke, and M. E. Tamisiea, "On seasonal signals in geodetic time series," *J. Geophys. Res., Solid Earth*, vol. 117, no. B1, Jan. 2012, Art. no. B01403.

[40] B. Chen, J. Bian, K. Ding, H. Wu, and H. Li, "Extracting seasonal signals in GNSS coordinate time series via weighted nuclear norm minimization," *Remote Sens.*, vol. 12, no. 12, p. 2027, Jun. 2020.

[41] J. Ran, J. Bian, G. Chen, Y. Zhang, and W. Liu, "A truncated nuclear norm regularization model for signal extraction from GNSS coordinate time series," *Adv. Space Res.*, vol. 70, no. 2, pp. 336–349, Jul. 2022.

[42] J. Gong, G. Chen, J. Bian, and Z. Wang, "Reconstruction of GPS coordinate time series based on low-rank Hankel matrix recovery," *Math. Geosci.*, vol. 56, no. 5, pp. 923–948, Jul. 2024.

[43] J. Morlet, G. Arens, E. Fourgeau, and D. Glard, "Wave propagation and sampling theory—Part I: Complex signal and scattering in multilayered media," *Geophysics*, vol. 47, no. 2, pp. 203–221, Feb. 1982.

[44] J. Morlet, G. Arens, E. Fourgeau, and D. Giard, "Wave propagation and sampling theory—Part II: Sampling theory and complex waves," *Geophysics*, vol. 47, no. 2, pp. 222–236, Feb. 1982.

[45] A. Grossmann and J. Morlet, "Decomposition of Hardy functions into square integrable wavelets of constant shape," *SIAM J. Math. Anal.*, vol. 15, no. 4, pp. 723–736, Jul. 1984.

[46] P. Goupillaud, A. Grossmann, and J. Morlet, "Cycle-octave and related transforms in seismic signal analysis," *Geoexploration*, vol. 23, no. 1, pp. 85–102, Oct. 1984.

[47] I. Daubechies, "Orthonormal bases of compactly supported wavelets," *Commun. Pure Appl. Math.*, vol. 41, no. 7, pp. 909–996, Oct. 1988.

[48] S. G. Mallat, "A theory for multiresolution signal decomposition: The wavelet representation," *IEEE Trans. Pattern Anal. Mach. Intell.*, vol. 11, no. 7, pp. 674–693, Jul. 1989.

[49] S. G. Mallat, "Multiresolution approximations and wavelet orthonormal bases of $L^2(\mathbf{R})$," *Trans. Amer. Math. Soc.*, vol. 315, no. 1, pp. 69–87, 1989.

[50] C. E. Heil and D. F. Walnut, "Continuous and discrete wavelet transforms," *SIAM Rev.*, vol. 31, no. 4, pp. 628–666, Dec. 1989.

[51] K. Ji, Y. Shen, and F. Wang, "Signal extraction from GNSS position time series using weighted wavelet analysis," *Remote Sens.*, vol. 12, no. 6, p. 992, Mar. 2020.

[52] S. Savchuk, S. Doskich, P. Gołda, and A. Rurak, "The seasonal variations analysis of permanent GNSS station time series in the central-east of Europe," *Remote Sens.*, vol. 15, no. 15, p. 3858, Aug. 2023.
[53] D. O. Trad and J. M. Travassos, "Wavelet filtering of magnetotelluric data," *Geophysics*, vol. 65, no. 2, pp. 482–491, Mar. 2000.
[54] N. Liu, W. Li, R. Tao, and J. E. Fowler, "Wavelet-domain low-rank/group-sparse destriping for hyperspectral imagery," *IEEE Trans. Geosci. Remote Sens.*, vol. 57, no. 12, pp. 10310–10321, Dec. 2019.
[55] C. Wang et al., "Translution-SNet: A semisupervised hyperspectral image stripe noise removal based on transformer and CNN," *IEEE Trans. Geosci. Remote Sens.*, vol. 60, 2022, Art. no. 5533114.
[56] Y. Long, X. Wang, M. Xu, S. Zhang, S. Jiang, and S. Jia, "Dual self-attention Swin transformer for hyperspectral image super-resolution," *IEEE Trans. Geosci. Remote Sens.*, vol. 61, 2023, Art. no. 5512012.
[57] P. Wang, H. Yao, B. Huang, H. Leung, and P. Liu, "Multiresolution analysis pansharpening based on variation factor for multispectral and panchromatic images from different times," *IEEE Trans. Geosci. Remote Sens.*, vol. 61, 2023, Art. no. 5401217.
[58] Y. Shen et al., "Spatiotemporal filtering of regional GNSS network's position time series with missing data using principal component analysis," *J. Geodesy*, vol. 88, no. 1, pp. 1–12, 2014.
[59] Y. Shen, F. Peng, and B. Li, "Improved singular spectrum analysis for time series with missing data," *Nonlinear Processes Geophys.*, vol. 22, no. 4, pp. 371–376, Jul. 2015.
[60] R. Tehranchi, K. Moghtased-Azar, and A. Safari, "Fast approximation algorithm to noise components estimation in long-term GPS coordinate time series," *J. Geodesy*, vol. 95, no. 2, Feb. 2021, Art. no. 18.
[61] D. A. Cucci, L. Voirol, G. Kermarrec, J.-P. Montillet, and S. Guerrier, "The generalized method of wavelet moments with eXogenous inputs: A fast approach for the analysis of GNSS position time series," *J. Geodesy*, vol. 97, no. 2, Feb. 2023, Art. no. 14.
[62] S. M. Kay and S. L. Marple, "Spectrum analysis—A modern perspective," *Proc. IEEE*, vol. 69, no. 11, pp. 1380–1419, 1981.
[63] D. H. Schoellhamer, "Singular spectrum analysis for time series with missing data," *Geophys. Res. Lett.*, vol. 28, no. 16, pp. 3187–3190, Aug. 2001.
[64] D. Mondal and D. B. Percival, "Wavelet variance analysis for gappy time series," *Ann. Inst. Stat. Math.*, vol. 62, no. 5, pp. 943–966, Oct. 2010.
[65] G. Foster, "Wavelets for period analysis of unevenly sampled time series," *Astronomical J.*, vol. 112, pp. 1709–1729, Oct. 1996.
[66] E. Ghaderpour and S. Pagiatakis, "Least-squares wavelet analysis of unequally spaced and non-stationary time series and its applications," *Math. Geosci.*, vol. 49, no. 7, pp. 819–844, 2017.
[67] E. Ghaderpour, "Least-squares wavelet analysis and its applications in geodesy and geophysics," Ph.D. dissertation, Dept. Earth Space Sci. Eng., York Univ., Toronto, ON, Canada, 2018.
[68] E. Ghaderpour, E. S. Ince, and S. D. Pagiatakis, "Least-squares cross-wavelet analysis and its applications in geophysical time series," *J. Geodesy*, vol. 92, no. 10, pp. 1223–1236, Oct. 2018.
[69] E. Ghaderpour and S. D. Pagiatakis, "LSWAVE: A MATLAB software for the least-squares wavelet and cross-wavelet analyses," *GPS Solutions*, vol. 23, no. 2, Apr. 2019, Art. no. 50.
[70] E. Ghaderpour, S. D. Pagiatakis, G. S. Mugnozza, and P. Mazzanti, "On the stochastic significance of peaks in the least-squares wavelet spectrogram and an application in GNSS time series analysis," *Signal Process.*, vol. 223, Oct. 2024, Art. no. 109581.
[71] D. B. Percival, *Wavelet Methods for Time Series Analysis*. Cambridge, U.K.: Cambridge Univ. Press, 2000.
[72] A. Klos, M. S. Bos, and J. Bogusz, "Detecting time-varying seasonal signal in GPS position time series with different noise levels," *GPS Solutions*, vol. 22, no. 1, Jan. 2018, Art. no. 11.
[73] Y. Meyer, *Wavelets and Operators*. Cambridge, U.K.: Cambridge Univ. Press, 1993.
[74] A. Agnieszka and D. Dawid, "Modeling seasonal oscillations in GNSS time series with complementary ensemble empirical mode decomposition," *GPS Solutions*, vol. 26, no. 4, Oct. 2022, Art. no. 101.
[75] A. R. Amiri-Simkooei, T. H. Mohammadloo, and D. F. Argus, "Multivariate analysis of GPS position time series of JPL second reprocessing campaign," *J. Geodesy*, vol. 91, no. 6, pp. 685–704, Jun. 2017.
[76] A. Vitti, "Sigseg: A tool for the detection of position and velocity discontinuities in geodetic time-series," *GPS Solutions*, vol. 16, no. 3, pp. 405–410, Jul. 2012.
[77] Y. Han and Y. Fu, "Analysis of GPS time series of height component," *Geomatics Inf. Sci. Wuhan Univ.*, vol. 28, no. 4, pp. 425–428.
[78] J. D. Scargle, "Studies in astronomical time series analysis. II. Statistical aspects of spectral analysis of unevenly spaced data," *Astrophys. J.*, vol. 263, pp. 835–853, Dec. 1982.
[79] W. H. Press, S. A. Teukolsky, W. T. Vettering, and B. P. Flannery, *Numerical Recipes in C++: The Art of Scientific Computing*, 2nd ed., Cambridge, U.K.: Cambridge Univ. Press, 2003.
[80] J. Bogusz and A. Klos, "On the significance of periodic signals in noise analysis of GPS station coordinates time series," *GPS Solutions*, vol. 20, no. 4, pp. 655–664, Oct. 2016.
[81] K. Ji, Y. Shen, N. Sneeuw, F. Wang, and Q. Chen, "Least squares Fourier filter for processing incomplete and heterogeneous GNSS position time series," *GPS Solut.*, vol. 29, no. 3, 2025, Art. no. 130.
[82] G. Strang and T. Q. Nguyen, *Wavelets and Filter Banks*. Cambridge, MA, USA: Wellesley-Cambridge, 1996.

Kunpu Ji received the B.S. degree in surveying engineering from the School of Geomatics Science and Technology, Nanjing Tech University, Nanjing, China, in 2017, and the M.S. and Ph.D. degrees in geodesy from the College of Surveying and Geo-Informatics, Tongji University, Shanghai, China, in 2020 and 2025, respectively.

His main research interests include geodetic inversion problem and geodetic time-series analysis.

Yunzhong Shen received the Ph.D. degree in geophysical geodesy from the Institute of Geodesy and Geophysics, Chinese Academy of Sciences, Wuhan, China, in 2000.

He is currently a Professor with the College of Surveying and Geo-Informatics, Tongji University, Shanghai, China. His primary research interests include the regularized solution to the ill-conditioned inverse problem of recovering a gravitational potential model from satellite-to-satellite tracking data and variance component and parameter estimation theory in mixed integer models of multisystem and triple-frequency Global Navigation Satellite System (GNSS) observations. His research interests include geodetic data processing on satellite positioning and satellite gravimetry.

Fengwei Wang received the B.S. degree in surveying and mapping engineering from Shandong University of Science and Technology, Taian, China, in 2011, the M.S. degree from East China University of Technology, Nanchang, China, in 2016, and the Ph.D. degree in geodesy from Tongji University, Shanghai, China, in 2021.

He is currently an Associate Professor with the College of Surveying and Geo-Informatics, Tongji University. His research interests include global sea-level change and temporal gravity field inversion.